Using $Z \to \tau\tau$ events to calculate tau ID scale factors using high p_T tau leptons

Diego Baron

Supervisor: Prof. Terry Wyatt

Examiner: Dr. Marco Gersabeck

Abstract

Different algorithms have been trained by the ATLAS collaboration to separate true hadronically decaying taus from QCD jets. The efficiency of these algorithms is compared in simulation and data and correction factors are derived to account for the differences that may arise from the simulation limitations. Our study makes use of $Z \to \tau_\mathrm{h} l$ events highly boosted in the transverse plane,, where $l = e, \mu$, to evaluate the performance of the tau-ID algorithms for high-p_T taus. The scale factors are defined as

$$C_\mathrm{ID} = \frac{\mathcal{E}_\mathrm{MC}}{\mathcal{E}_\mathrm{Data}},$$

where $\mathcal{E}$ is the efficiency of the algorithms measured in the data and the simulation. The value obtained for the scale factors for the classifier *tight-ID* working point in the muon-tau final state is $C_\mathrm{Tight\text{-}ID} = 0.989 \pm 0.012(\mathrm{stat}) \pm 0.024(\mathrm{lumi}) \pm 0.028(\mathrm{sys})$ and $C_\mathrm{Tight\text{-}ID} = 0.974 \pm 0.014(\mathrm{stat}) \pm 0.023(\mathrm{lumi}) \pm 0.029(\mathrm{sys})$ for the electron-tau final state.

Contents

List of Figures

List of Tables

1   Introduction

The tau lepton has a proper decay length of 87 μm [1]. For this reason, tau leptons usually decay before they can reach the innermost layer of the ATLAS detector. Thus, only the decay products of the tau leptons can be observed. The tau lepton mass of 1.777 GeV make this particle the only lepton that can decay into hadrons [1]. Tau decays can be either leptonically ($\tau \rightarrow \nu_\tau \nu_l l$, $l = e, \mu$) or semi-hadronically ($\tau \rightarrow \nu_\tau$hadrons), the latter ones are commonly referred simply as hadronic tau decays (τ_h). Muons and electrons from leptonic tau decays do not have enough kinematical features that can make them easily distinguishable from prompt muons or electrons. In the case of hadronic tau decays, which represent approximately a branching fraction of 65%, the decay modes include one or three charged pions. Therefore, the signature of these decays are jets with one or three tracks, with a charge correlation and being more collimated than jets initiated from quark or gluon radiation.

For this reason, algorithms trained to identify true τ_h and separating them from misidentified τ_h candidates, originating from QCD processes, have been developed [2]. The most novel of these algorithms is a recurrent neural network (RNN) that uses track and calorimeter information in order to classify true and fake τ_h candidates. The RNN is now used as the default tau identification criteria for the data recorded by the ATLAS experiment from 2015 to 2018 and has been used also in tau lepton triggers of 2018.

When the efficiency of the RNN algorithm is measured in data and simulation, a correction factor is derived and then applied to the simulation in order for the signal efficiency to agree between data and simulation. In this report, we summarize the progress that has been done during the first year of the PhD student Diego Baron. The work is aimed to measure the correction factors for tau identification in the high-p_T regime using $Z \rightarrow \tau_h \tau_{lep}$ events.

The report is structured as follows. Chapter 2 is a short review of the Standard Model and the physics of the tau lepton. Chapter 3 describes the ATLAS experiment and the tau reconstruction and identification. In Chapter 4 the analysis methodology and the event selection is presented. Some preliminary results and a discussion is presented in Chapter 5. Finally, in Chapter 6 conclusions and prospects are discussed.

2   The Standard Model and Lepton Universality Tests

This chapter begins with a short description of the Standard Model (SM), followed by a discussion about the Z boson production at the Large Hadron collider. Finally, a review of the tau lepton properties is presented. These include the nature of this particle, its interactions with the other SM particles, its main decay modes and the physics implications of the so called Lepton Universality (LU), one of the SM predictions.

2.1   The Standard Model

The Standard Model (SM) is a theory about the fundamental constituents of matter and the interactions between them. Four fundamental interactions are known: gravitational, electromagnetic, weak and strong interactions. The SM is based on the framework of Quantum Field Theory (QFT), in which particles are classified as *bosons* or *fermions*, which correspond to particles with integer and half-integer spin respectively. Fermions form matter and they can interact with each other via the exchange of bosons, which are the force carriers. Three fundamental forces are described by the SM. The strong interaction is explained by a theory called quantum chromodynamics (QCD) [3] which relies on the principle of gauge invariance under the $SU(3)_c$ group. The force carriers of the QCD are called *gluons*. The electromagnetic and weak interactions are unified in the SM and this theory is known as the electroweak (EW) theory [4, 5, 6]. In this sector of the SM the fields are invariant under $SU(2)_L \times U(1)_Y$ group. The force carriers of the electroweak interactions are the $Z^0, W^\pm$ bosons and the *photon* (γ). The gravitational interaction is not described by the SM.

Fermions in the SM are classified into *quarks* and *leptons* where the latter do not feel the strong interaction. There are six quarks grouped into three generations with increasing masses. Thus, the heavier generations can decay into the lighter ones. There are also six leptons grouped in three generations. Each generation is heavier than the previous one. There are three charged leptons: the electron (e), the muon (μ) and the tau (τ); and their associated neutral partners, the *neutrinos* (ν). In order to give mass to the SM particles the Higgs mechanism was proposed in the 60's [7, 8, 9]. The existence of the Higgs boson is a further consequence of the Higgs mechanism. The Higgs boson is the only spin-0 particle in the SM. Fig.1 shows the SM particle content.

2.2   Z boson production at the LHC

Since the discovery of the Z and W bosons at the UA1 and UA2 experiments [11, 12, 13, 14], the Z boson has been the subject of multiple measurements in proton-proton and electron-positron colliders. The Z boson mass $m_Z = 91.1875 \pm 0.0021$ GeV and its decay width $\Gamma_Z = 2.4952 \pm 0.0023$ GeV have been measured to outstanding precision [15]. The braching ratios of the Z boson are well known; they are presented in Table 1. In contrast to electron-positron colliders, the momentum of partons in proton-proton collisions is not precisely known. Thus, parton density functions (PDFs) are used to describe the proton structure in a phenomenological way. These functions are written as $f_{a/A}(x, Q^2)$ and represent the probability density for a parton a to have a fraction $x = \frac{p_a}{p_A}$ of the proton momentum p_A. Q is the energy scale of the scattering process. In this case, the cross

Decay mode	Branching fraction (%)
e^+e^-	3.363 ± 0.004
$\mu^+\mu^-$	3.366 ± 0.007
$\tau^+\tau^-$	3.370 ± 0.008
Invisible	20.00 ± 0.06
Hadrons	69.91 ± 0.06

Table 1: Z boson branching fractions. Number taken from [1].
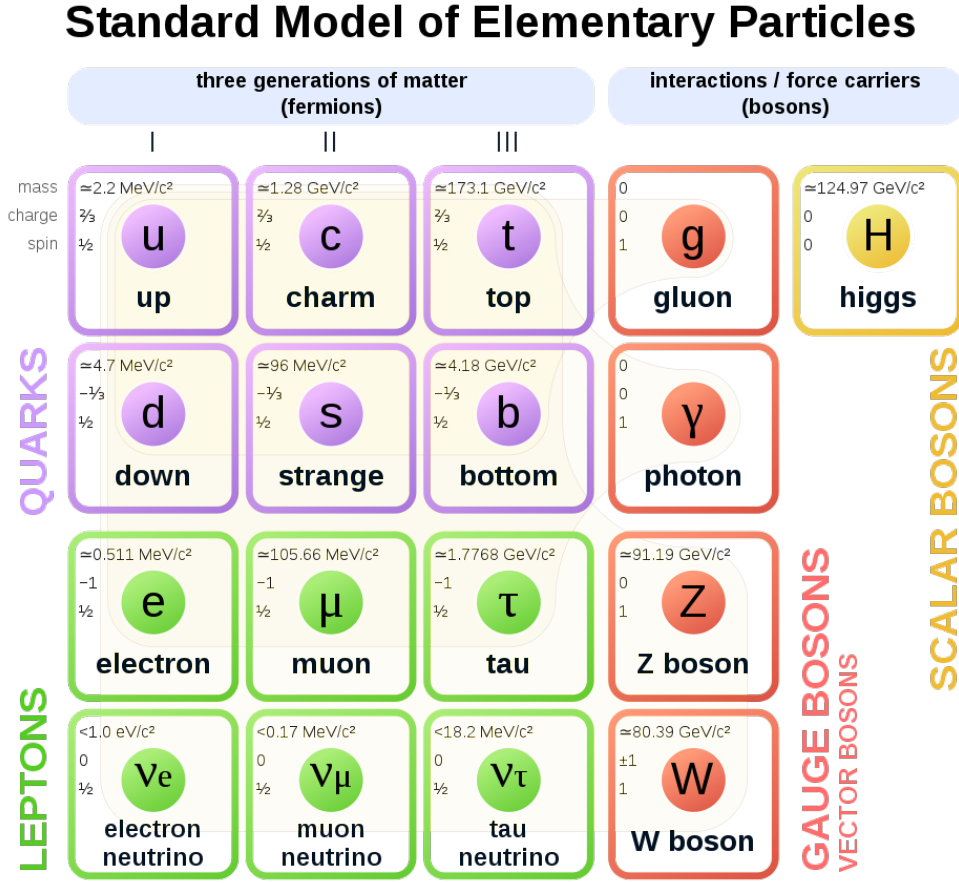
Figure 1: The particle content of the Standard Model. Taken from [10].

section of two protons going to a final state n will be

$$\sigma_{p_A p_B \to n} = \sum_q \int dx_a dx_b f_{a/A}(x_a, Q^2) f_{b/B}(x_b, Q^2) \times [\sigma_0 + \alpha_s \sigma_1 + \ldots]_{ab \to n}. \tag{1}$$

The sum is made over all the partons. σ_0 is the tree level parton-parton cross section and σ_1 are the QCD corrections to first order. A diagram of the production of the Z boson in proton-proton collisions is shown in Fig.2. The main process contributing to Z boson production is the Drell-Yan process, where a quark-antiquark ($q\bar{q}$) pair annihilate, produce a Z boson and it subsequently decays into a pair of fermions. In this case, the transverse momentum (p_T) of the Z boson comes from the intrinsic p_T of the partons. Nevertheless, this has been experimentally determined with a value of $< k_T >= 0.76$ GeV [16] and is not large enough to explain the measured Z boson p_T distribution that peaks at a few GeV and has a tail that extends at values $p_T \gg m_Z$ [17, 18].

To explain this kinematic feature we have to look at the other ways the Z boson can be produced in *pp* collisions. First quark-gluon (qg) scattering, where the Z boson recoils against the quark radiated by the gluon in the initial state, this process is illustrated in Fig.3a. In the other hand, we could also have a gluon being radiated before $q\bar{q}$ annihilation takes place, having the Z boson recoiling against what is called *initial state radiation* (ISR), as is shown in Fig.3b. High transverse momentum partons lead to the production of collimated showers of hadrons, called jets, that are subsequently detected as energy deposits in the calorimeters of the particle detectors.
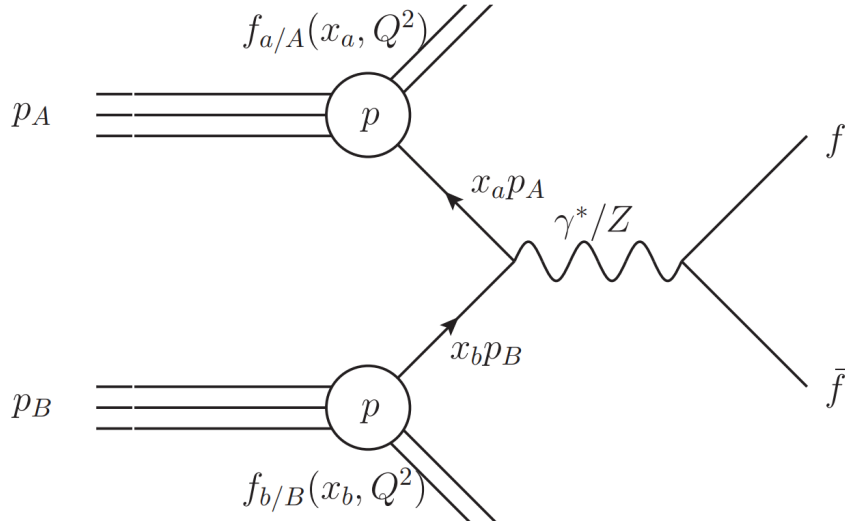
Figure 2: Illustration of the production of a Z boson in pp collisions via quark-antiquark annihilation.
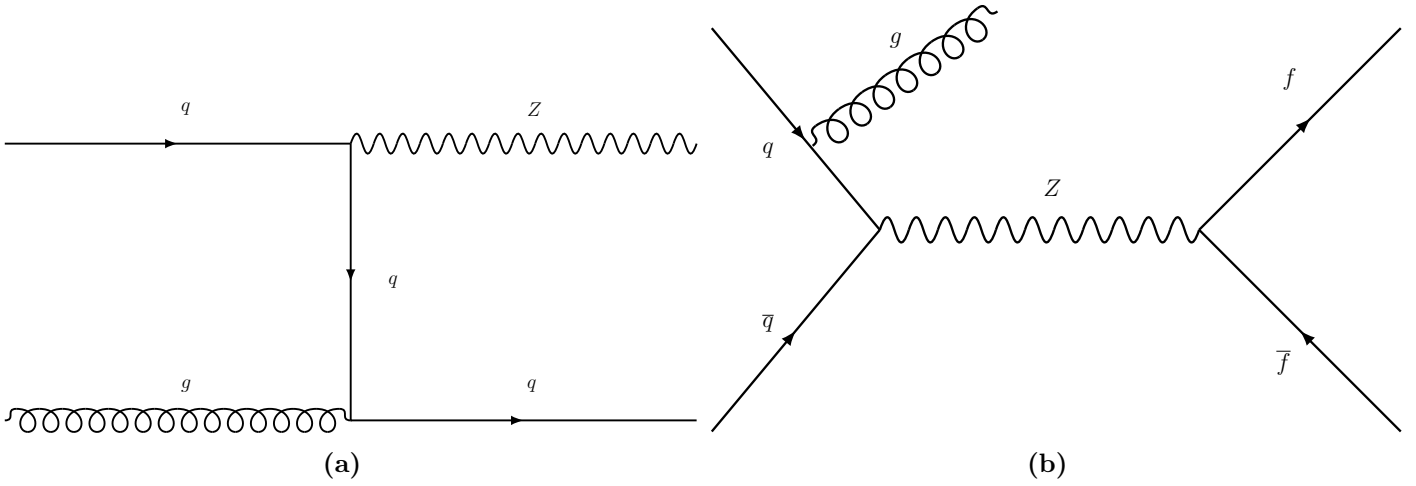
Figure 3: qg Z boson production with FSR (a) and $q\bar{q}$ annihilation with gluon ISR (b).

2.3 The Tau Lepton

The tau is a spin-$\frac{1}{2}$ charged particle that belongs to the family of leptons. The first hints of the tau existence came from experiments conducted at the Stanford Linear Accelerator Center and Lawrence Berkeley National Laboratory [19]. They discovered 64 events of the form:

$$e^+ + e^- \rightarrow e^\pm + \mu^\mp + \geq 2 \text{ undetected particles,} \tag{2}$$

for which there was no conventional explanation at the time. Later on, it was discovered that these events came from the production of a pair of new particles, two taus that subsequently decayed into one electron, a muon and four neutrinos. Events like,

$$e^+ + e^- \rightarrow \tau^+\tau^- \rightarrow e^\pm + \mu^\mp + 4\nu, \tag{3}$$

were later explored to derive tau mass and spin, confirming the existence of a third generation of leptons. The tau has a mass of 1776.86 ± 0.12 MeV [1], which allows it to decay not only into the other lighter lepton generations (*leptonic tau decays*), as shown on Fig.4 , but into hadrons. As we said on section 2.2 hadrons are particles made of quarks. All the decay channels of the tau containing hadrons in the final state are called *hadronic tau decays*. Strictly speaking this is a semi-hadronic decay mode because of the presence of the neutrino. Nonetheless, from now on we will refer to these processes with the commonly used term *hadronic tau decays*. An example of this decay mode is shown in Fig.5. The branching fraction for hadronic and leptonic tau decay modes is defined as
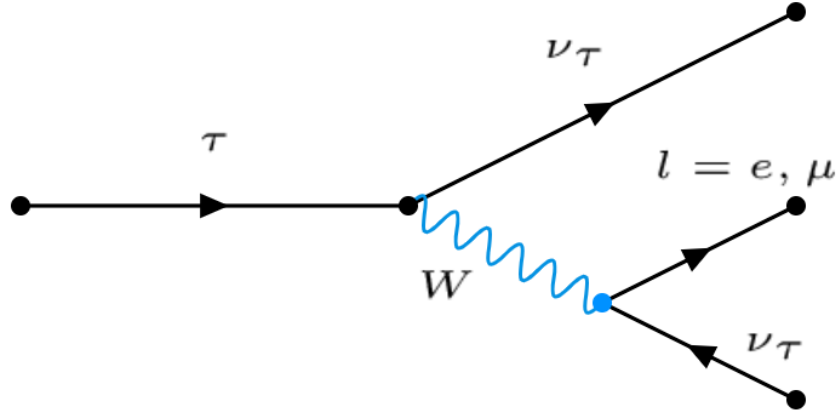
Figure 4: Tau leptonic decay mode. Tau lepton is kinematically allowed to decay into muons or electrons, note that in this decay mode two neutrinos of different flavour are produced.
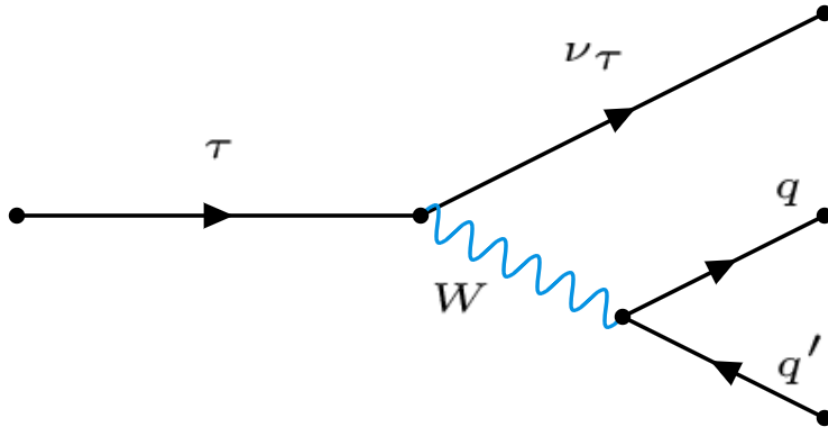
Figure 5: Tau hadronic decay mode. The tau lepton is kinematically allowed only to decay into hadrons containing up, down and strange quarks. This results on final states containing multiple pions or kaons [20].

$$\beta(\tau \to X\nu_\tau) = \frac{\Gamma(\tau \to X\nu_\tau)}{\Gamma_{\text{tot}}}, \tag{4}$$

where X could be any number of leptons or hadrons and Γ_{tot} is the total decay width for the tau. Naively, if we were to estimate it we could argue that the contribution from the hadronic decays triples the contribution for one of the leptonic modes. This is because in any hadronic decay, we would have to count 3 different diagrams, like the one in Fig.5 because of the three colour possibilities for the quarks.

Thus,

$$\beta(\tau \to l\nu_l\nu_\tau) \approx 20\% \qquad l = e, \mu; \tag{5}$$

$$\beta(\tau \to X\nu_\tau) \approx 60\% \qquad X = \text{hadrons+neutrinos}. \tag{6}$$

In fact, this naive estimation is not bad. Actual values for the leptonic branching ratios are [1]:

$$\beta(\tau \to e\nu_e\nu_\tau) = 17.82 \pm 0.04\% \tag{7}$$

$$\beta(\tau \to \mu\nu_\mu\nu_\tau) = 17.39 \pm 0.04\%. \tag{8}$$

The reason for the difference in the estimation are the QCD corrections in the hadronic decays [21]. The small difference between the leptonic branching fractions is due to the mass difference between the muon and the electron.

Decay mode	Branching fraction
$\pi^{\pm}\nu_{\tau}$	11.1 %
$\pi^{\pm}\pi^0\nu_{\tau}$	25.4%
$\pi^{\pm} \geq 2\pi^0\nu_{\tau}$	9.1%
$3\pi^{\pm}\nu_{\tau}$	9.1%
$3\pi^{\pm} \geq 1\pi^0\nu_{\tau}$	4.6%
others	5.5%

Table 2: Branching fractions for hadronic tau decay modes [1].

On the other hand, the hadronic decays of the tau are more varied and can contain many more particles in the final states. The vast majority of hadronic tau decays have charged or neutral pions in the final states, but more exotic decays including kaons also happen. Branching fractions for the most important tau hadronic decays are showed in Table 2.

2.4 Lepton Universality

The SM predicts that all charged leptons (e, μ, τ) interact via the electroweak force and explains that these interactions can be seen as the interchange of *vector bosons*, the photon (γ) and the W and Z bosons. Specifically, in the SM the form of the interaction does not depend on the lepton generation. This feature of the SM is called *lepton universality* and is the fact that the couplings of the electrons, muons and taus to the electroweak bosons are identical.

For instance, tau leptonic decay widths present a great opportunity to test lepton universality hypothesis. If we start considering muon decay, at low energies we can consider this process to be a point like interaction well described by Fermi theory [22]. In this case, if we approximate the electron and neutrinos as being massless particles, a dimensionally correct expression for the width is of the form

$$\Gamma(\mu \to e + \nu_e + \nu_\mu) = K G_F^2 m_\mu^5, \tag{9}$$

where $G_F = 1.1666 \times 10^{-5}$ GeV^{-2} is the Fermi coupling constant and K is a constant that depends on the form of the interaction. If we assume that lepton universality holds, the respective widths for the tau leptonic decay modes, will have the form

$$\Gamma(\tau \to e + \nu_e + \nu_\tau) = K G_F^2 m_\tau^5, \tag{10}$$

$$\Gamma(\tau \to \mu + \nu_\mu + \nu_\tau) = \Gamma(\tau \to e + \nu_e + \nu_\tau), \tag{11}$$

which explains why to a good approximation leptonic branching fractions for tau decay are equal. Moreover, we can obtain a relation between tau and muon lifetimes. We know that,

$$\tau l = \frac{1}{\Gamma_{\text{Tot}}} = \frac{\beta(l \to e\nu_e\nu_l)}{\Gamma(l \to e\nu_e\nu_l)}, \tag{12}$$

also that $\beta(\mu \to e\nu_e\nu_\mu) = 1$ and taking into account eq.(7) we can take the ratio between eq.(12) for $l = \tau, \mu$ to obtain

$$\frac{\tau_\tau}{\tau_\mu} = \frac{\beta(\tau \to e\nu_e\nu_\tau)}{\beta(\mu \to e\nu_e\nu_\mu)} \left(\frac{m_\mu}{m_\tau}\right)^5 = (1.328 \pm 0.004) \times 10^{-7}. \tag{13}$$

This is consistent with the experimental lifetimes ratio of $(1.3227 \pm 0.0005) \times 10^{-7}$ [23]. This agreement on lifetimes that differ by seven orders of magnitude is a good proof that lepton universality holds on W decays at the tau mass scale.

Very precise tests of LU have been done by $e^- e^+$ colliders (LEP1, SLC and LEP2). Measurements of the

ratios between the leptonic decay widths of the Z boson have been performed and are consistent with the SM [15]:

$$\frac{\Gamma(Z \to \mu^+\mu^-)}{\Gamma(Z \to e^+e^-)} = 1.0009 \pm 0.0028, \tag{14}$$

$$\frac{\Gamma(Z \to \tau^+\tau^-)}{\Gamma(Z \to e^+e^-)} = 1.0019 \pm 0.0032. \tag{15}$$

LU has also been tested in W boson decays. A combination of measurements made by different experiments of the branching fractions between the first two families of leptons are consistent with SM predictions [21]:

$$\frac{\beta(W^- \to e^-\bar{\nu}_e)}{\beta(W- \to \mu^-\bar{\nu}_\mu)} = 1.004 \pm 0.008. \tag{16}$$

However, measurements including the third lepton family, apart from being less precise due to the more challenging reconstruction of the τ lepton final states are in tension with SM [24]:

$$\frac{\Gamma(W^- \to \tau^-\bar{\nu}_\tau)}{\Gamma(W^- \to e^-\bar{\nu}_e)} = 1.063 \pm 0.027, \tag{17}$$

$$\frac{\Gamma(W^- \to \tau^-\bar{\nu}_\tau)}{\Gamma(W^- \to \mu^-\bar{\nu}_\mu)} = 1.070 \pm 0.026. \tag{18}$$

These results show that LU between the two first lepton family holds with a precision of 0.3% and 0.8% in Z and W decays respectively. Constraints between the third and the other two generations of leptons are of similar precision on Z boson decays (0.3%), but ten times worse for W boson decays (3%) and somewhat in tension with SM prediction.

Furthermore, measurements from LHCb, BaBar and Belle experiments have shown consistent deviations from the SM predictions [25]. These experiments have independently measured a deviation on $\bar{B}$ meson semi-leptonic branching ratios, specifically:

$$R_D = \frac{\beta(\bar{B} \to D\tau^-\bar{\nu}_\tau)}{\beta(\bar{B} \to De^-\bar{\nu}_e)} \tag{19}$$

$$R_{D^\star} = \frac{\beta(\bar{B} \to D^\star\tau^-\bar{\nu}_\tau)}{\beta(\bar{B} \to D^\star e^-\bar{\nu}_e)}. \tag{20}$$

The combined results for the different experiments are shown in Fig.6. These measurements represent a 3.08 σ deviation from the SM predictions, but even though they represent a hint of new physics, higher statistical precision will be needed to confirm this results. Future analysis from experiments like LHCb and Belle II with larger available datasets will be very important to untangle this situation.
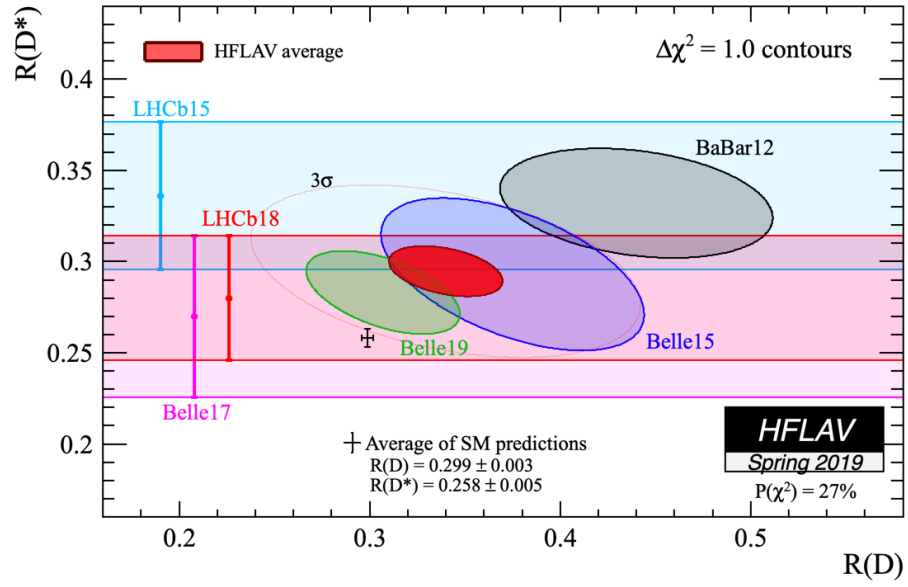
Figure 6: Combined results from BABAR, Belle and LHCb with 1-σ contour. The average calculated by the Heavy Flavour Averaging Group [26] is compared with the SM predictions.

3 Tau Reconstruction and Identification in ATLAS

In this chapter, a review of the ATLAS detector at the Large Hadron Collider and a description of the reconstruction and identification of hadronic tau decays in ATLAS are presented.

3.1 The LHC and the ATLAS experiment

The Large Hadron Collider (LHC) is the largest particle accelerator currently operated by the European Organization for Nuclear Research (CERN). The LHC uses a 27 km tunnel where 2090, 15 m long, dipolar superconducting magnets bend the trajectories of two proton beams going in opposite directions. Each of the magnets is capable of producing a 8.33 T magnetic field and thus bending protons with an energy up to 7 TeV. The magnets are cooled down to 1.9 K in order to reach the superconducting state and the vacuum inside the beam pipes is of the order of 10^{-9} mbar. During LHC Run II, proton beams were accelerated to an energy of 6.5 TeV and they were collided in 4 interaction points where the detector experiments are located.

One of these experiments is the ATLAS (A Toroidal LHC ApparatuS) detector. It is a multi-purpose particle detector, capable of discovering new physics but also to perform high precision SM measurements. A complete description of the ATLAS detector design can be found at [27]. ATLAS is a cylindrical detector composed by sub-detectors arranged in shells. The most inner layers are surrounded by a superconducting solenoid that generates a 2 T solenoidal magnetic field. ATLAS uses a right-handed coordinate system with its origin at the interaction point (IP) in the centre of the detector, the z-axis points along the beam pipe. The x-axis points towards the centre of the LHC ring and the y-axis in the vertical direction. The angle ϕ is defined in the $x - y$ plane and pseudorapidity is defined in terms of the polar angle θ as $\eta = -\log\tan(\theta/2)$. The angular distance is measured in units of $\Delta R \equiv \sqrt{(\Delta\phi)^2 + (\Delta\eta)^2}$.

The most inner detector is responsible for track and vertex reconstruction and it consist of silicon pixel, silicon microstrip and transition radiation tracking detectors. The system has a coverage of $|\eta| < 2.5$. The tracker system is followed by a lead/liquid-argon electromagnetic calorimeter (EC) and a steel/scintillator-tile hadron calorimeter (HC) that provide energy measurements with high granularity for electromagnetic showers and hadrons. The end-cap and forward EC and HC use LAr technology detectors and extend up to a $|\eta = 4.9|$ region. The outermost detection system is a muon spectrometer (MS) that takes advantage of the bending power of a system of three air-core toroidal superconducting magnet systems.

Electrons are reconstructed matching a track in the inner tracking system and energy deposits in the EM calorimeter. Electrons have also different ID working points associated with them. More information on the electron reconstruction and ID can be find at [28]. Muon reconstruction is as well independently done at the inner tracking detector and in the MS. Tracks in each subdetector are then matched and depending on different subdetector information and reconstruction algorithms muons are classified in different types [29]. Hadronic jets are built from energy deposits in the calorimeters, using the anti-k_t algorithm with radius parameter $R = 0.4$ [30]. High-level tagging algorithms combine the outputs from different low-level algorithms in order to tag the flavour of the jets. In the case of bottom flavour jets (b-jets) the MV2 algorithm is used [31]. It takes into account features like the impact parameter, which is the shortest distance between the primary vertex (PV) and the z-axis. The PV vertex is defined as the one having the highest sum of the squared transverse momenta of the tracks associated with the same vertex [32, 33]. More information on the b-tagging algorithms can be find at [34].

3.2 Tau Reconstruction and Identification on the ATLAS detector

Leptonically decaying taus (τ_{lep}), may have a higher impact parameter and tend to have a softer p_T spectrum compared with prompt muons or electrons coming from W or Z boson decays. In practice, the small differences in these variables make it difficult to differentiate between τ_{lep} and prompt muons or electrons. In the case of

hadronically decaying taus (τ_{had}), as we will see, there are a lot more variables we could use to tag the presence of a τ_{h}.

As we saw in section 2.3, τ_{h} decays can be classified in 1-prong or 3-prong, depending on the number of charged particles in the decay. A detailed review of the reconstruction procedure for τ_{h} is discussed in [35]. τ_{h} candidates are seeded by jets using the anti-k_t algorithm [30] with a distance parameter of 0.4. Jets are required to have $p_T > 10$ GeV and $|\eta| < 2.5$. Candidates between the barrel and forward calorimeter ($1.37 < |\eta| < 1.52$) are excluded due to poor instrumentation in this region.

The axis of the seed jet is defined by the energy-weighted barycentre of all clusters of calorimeter cells, called *TopoClusters* [36]. The τ_{h} vertex is selected as the one having the highest p_T sum of all the tracks with $p_T > 0.5$ GeV within a cone of $R = 0.2$ around the seed jet axis. Tracks within a cone of $R = 0.4$ are classified with a set of boosted decision trees (BDTs) into core and isolation tracks, the number of core tracks defines the number of prongs. Candidates with neither one or three tracks are rejected. Additionally, the sum of the charge of the tracks is required to be ± 1.

The tau reconstruction algorithm does not sufficient provide discrimination against jets that could mimic the signal of a τ_{h} decay in the detector. Therefore, algorithms that perform this task have been developed. Previously, a BDT was used to discriminate jets against τ_{h}. Recently, a recurrent neural network (RNN) classifier that provides improved performance compared with the BDTs is used [2].

The RNN makes use of a set of variables like: τ_{h} track features, information about energy deposits on the calorimeters clusters and high level features like the mass of the τ_{h} candidate tracks. These variables are used to exploit the differences in the shapes of the showers between τ_{h} and jets. In general, τ_{h} showers tend to be more collimated and to have fewer tracks than jets. A representation of this is shown in Fig.7.
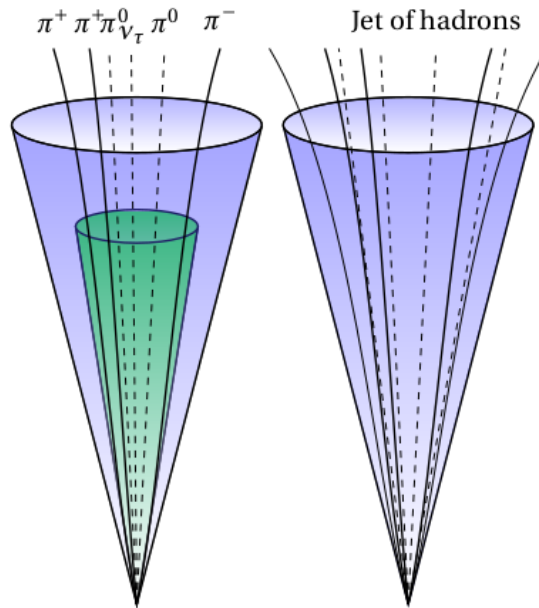
Figure 7: Graphic representation that shows the main differences between a 3-prong τ_{h} and a jet originated from quark or gluon radiation (QCD jets). Charged hadrons are shown as thick lines and dashed lines represent neutral particles. The green cone is drawn to depict how τ_{h} product decays are more collimated. Taken from [37].

Separate algorithms are trained for 1-prong and 3-prongs. The final RNN score assigned to each candidate corresponds to the fraction of rejected true τ_{h}, independent of p_T and number of interactions per bunch crossing (pileup). Four working points with increasing background rejection are defined to be used in physics analysis. The working points and background rejection factors are shown in Table 3. A plot comparing the true τ_{h} selection efficiency versus the background rejection power for the RNN and BDT algorithm is shown in Fig.8, the performance of the RNN is better than the BDT classifier. Finally, the distribution for the RNN score for

true and fake τ_h is shown in Fig.9, for both 1-prong and 3-prong decays.

Working point	Singal efficiency (%)		BG rejection BDT		BG rejection RNN	
	1-prong	3-prong	1-prong	3-prong	1-prong	3-prong
Tight	60	45	40	400	70	700
Medium	75	60	20	150	35	240
Loose	85	75	12	61	21	90
Very loose	95	95	5.3	11.2	9.9	16

Table 3: Working points with their corresponding true τ_h selection efficiency and the background rejection factors [2]. The scores are shown for both RNN and BDT algorithms.
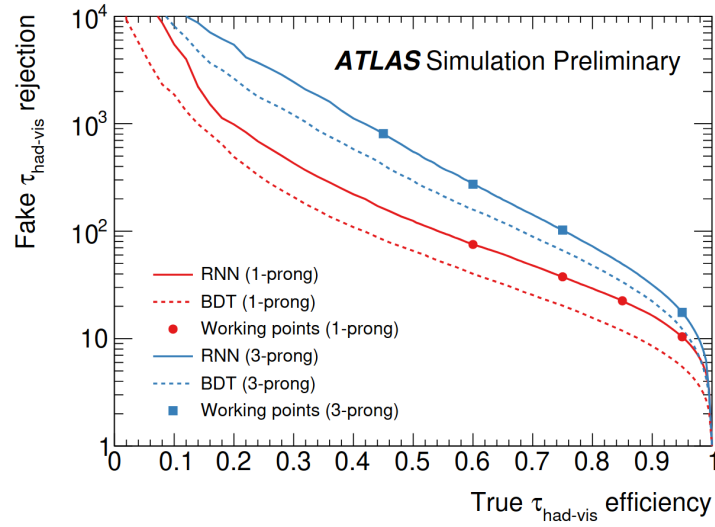
Figure 8: Comparisson between the performance of BDT and RNN algorithms. Working points are shown as solid dots. Notice there is a trade off between true τ_h efficiency and background rejection power. Taken from [2].
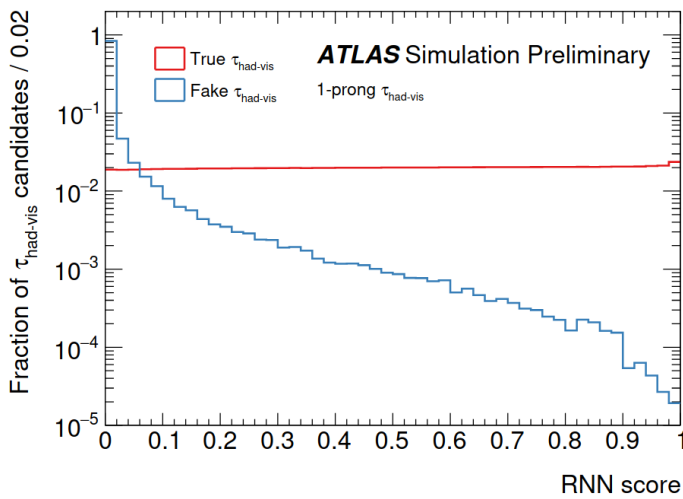
(a)
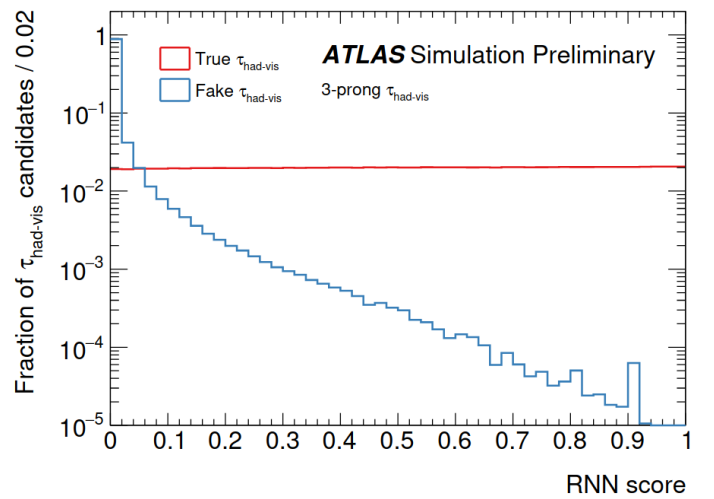
(b)

Figure 9: Distribution of the RNN scores for true and fake τ_h candidates for 1-prong (a) and 3-prong (b) cases. Taken from [2].

4 $Z \to \tau_\mathrm{h}\tau_\mathrm{lep}$ tag and probe study

This chapter describes the analysis methodology of using $Z \to \tau\tau$ events to measure Monte Carlo correction factors for tau identification algorithms in the high-p_T region.

As we saw in the previous section different working points are defined for RNN score relative to the efficiency of selecting true τ_h candidates. When the efficiency of the working points is measured in data and simulation, a correction factor is derived and then applied to the simulation in order for the signal efficiency to agree between data and simulation [38]. Because of the top quark mass, $t\bar{t}$ events are used as a source of high momentum taus for measuring correction factors on the high-p_T bins. But as we already saw in section 2.4, Lepton universality may not hold in W decays. For that reason our study is aimed to use $Z \to \tau\tau$ events for deriving and cross checking simulation correction factors in the high-p_T region.

4.1 Signal events

The type of $Z \to \tau\tau$ events we consider as signal for this study are when one the taus decays hadronically and the other leptonically, either into an electron or a muon ($Z \to \tau\tau \to \tau_h + l = \mu, e$). Thus, our final states will include a τ_h candidate and a lepton $l = e, \mu$. The presence of this lepton will be used as our tag. Generally, in $Z \to \tau\tau$ events, the taus are produced back to back and their p_T spectrum falls sharply. One way to select events where the taus are boosted in the transverse plane is to look for events where the opening angle in the transverse plane between the taus ($\Delta\phi(\tau_\mathrm{h}, \tau_\mathrm{lep})$) is more acute. A depiction of the topologies of our signal events is shown in Fig.10. For these events, the missing transverse momentum ($\not{E}_T$) is assumed to come from the neutrinos produced in the decays of the tau leptons. Due to the fact that two neutrinos are produced in the leptonic decay mode we expect our events to have a larger $\not{E}_T$ component along the τ_lep direction.

We classify our events in two types of topologies. First, events where the $\not{E}_T$ is inside the opening angle between the visible objects. In this kind of events we assume the missing energy is due to a pair of neutrinos flying in the same direction as the visible objects. This is shown in Fig.10a. In this case, we solve the following equation to obtain the momentum of the neutrinos:

$$\vec{p}_{T_{\nu_l}} + \vec{p}_{\nu_h} = \vec{\not{E}_T},\tag{21}$$

given the following set of constraints (*collinear approximation*):

$$\phi(\nu_l) = \phi(l),\tag{22}$$
$$\phi(\nu_h) = \phi(\tau_\mathrm{h}),\tag{23}$$
$$\eta(\nu_l) = \eta(l),\tag{24}$$
$$\eta(\nu_h) = \eta(\tau_\mathrm{h}).\tag{25}$$

The second case is when the $\not{E}_T$ is outside the angle formed by the visible objects, as is shown in Fig.10b. In this case the assumption is that only one neutrino is responsible for the majority of the $\not{E}_T$, a neutrino flying in the direction of the visible object that is closest to the $\not{E}_T$. We use the following equations to obtain the neutrino momentum:

$$p_{T_\nu} = \not{E}_T \cos(\Delta\phi(\tau_\mathrm{closer}, \not{E}_T)),\tag{26}$$
$$\phi(\nu) = \phi(\tau_\mathrm{closer}),\tag{27}$$
$$\eta(\nu) = \eta(\tau_\mathrm{closer}),\tag{28}$$

where τ_{closer} stands for the visible object closest to the direction of the missing energy.
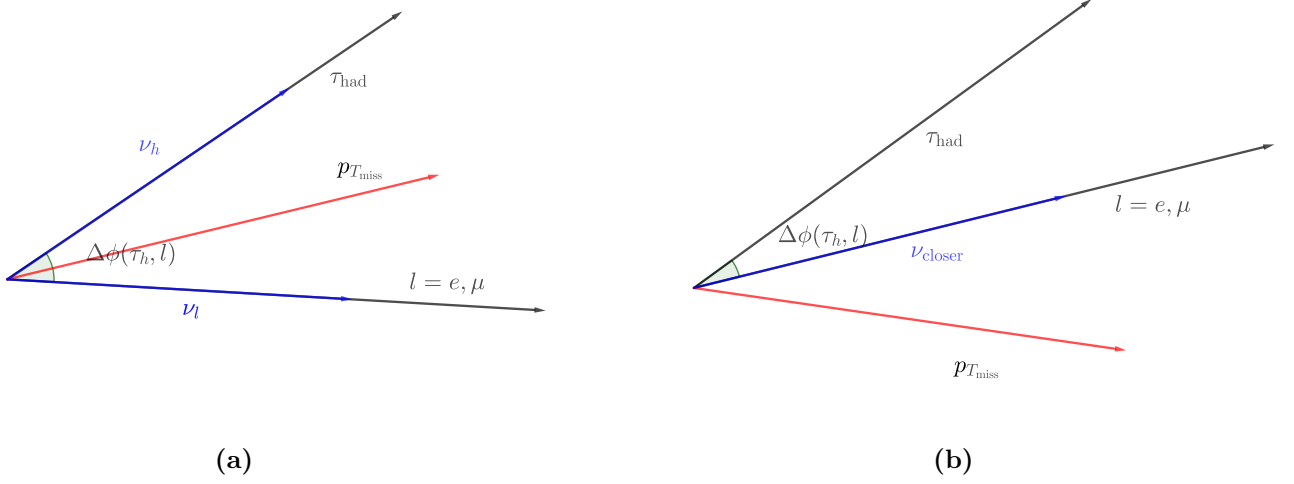
Figure 10: The two different types of topologies that define signal events. On the left, when the missing energy is between the visible objects two neutrinos are assumed to be responsible for all the missing energy. On the right, only one neutrino is assumed to be flying on the direction of the visible object closest to the missing energy.

We define a variable called Ω in order to classify our events in the different topologies already described. First we define:

$$\omega = \frac{\Delta\phi(\tau_{\text{closer}}, \not{E}_T)}{\Delta\phi(\tau_{\text{h}}, \tau_{\text{lep}})}, \tag{29}$$

then,

- when $\not{E}_T$ is inside the opening angle between the visible objects but closer to τ_{h}:

$$\Omega = \omega, \tag{30}$$

- when $\not{E}_T$ is still inside, but closer to τ_{lep}:

$$\Omega = 1 - \omega. \tag{31}$$

- If $\not{E}_T$ is outside and closer to τ_{h}:

$$\Omega = -\omega, \tag{32}$$

- and finally, if $\not{E}_T$ is outside and closer to τ_{lep}:

$$\Omega = \omega + 1. \tag{33}$$

Thus, Ω is a continuous variable that give us information on the topology of the event. When $\not{E}_T$ is inside the visible system it has values in the interval [0,1]. It is exactly 0 when $\not{E}_T$ is in the τ_{h} direction and 1 when $\not{E}_T$ is in the τ_{lep} direction. Ω has negative values when $\not{E}_T$ is outside and closer to the τ_{h} candidate and has positive and values greater than 1 when is outside and closer to the τ_{lep}. A diagram describing the Ω values is shown in Fig.11.
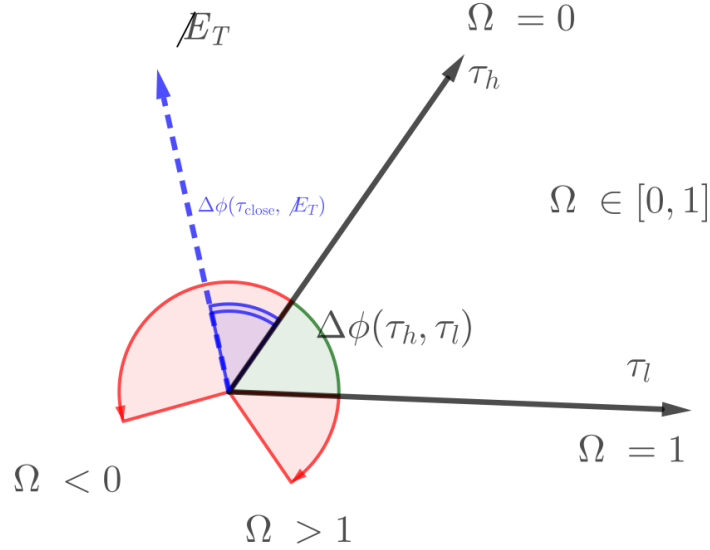
Figure 11: Graphical representation of the different values of Ω depending on the region where the $\not{E}_T$ is located in the event.

As we will see later the event classification into these different types of topologies will allow us to reconstruct and exploit kinematical variables as the invariant mass of the di-tau system, the Z boson transverse momentum (Z_{p_T}) and the angular distribution of the objects in the event.

4.2 Monte Carlo and Data Samples

The data used for this study has been recorded during the Run-II of the LHC. It corresponds to the 2015-2018 data taking period, the total integrated luminosity corresponds to 139.2 fb^{-1} of proton-proton collisions at a centre-of-mass energy of $\sqrt{s} = 13$ TeV.

Monte Carlo (MC) samples are used for signal and background simulation. For $Z \to \tau\tau$ events two MC samples are used, Powheg+Pythia8 and Sherpa. For the rest of the samples Powheg+Pythia8 is used. Table 4 shows the MC generators used for each process.

4.3 Event Selection

In order to select $Z \to \tau_h\tau_{lep}$ events, our basic selection includes events with exactly one τ_h candidate and one lepton, a muon or an electron. The τ_h and lepton pair need to have opposite charge. As we said, the presence of the lepton will be used as our tag, thus, a lepton trigger is required to be fired with an online requirement on the $p_T(\mu) \geq 20$ ($p_T(e) \geq 24$) GeV for 2015 data taking period. For 2016-2018 the online requirement is $p_T(\mu, e) \geq 26$ GeV. The muons are required to pass a *medium* ID requirement and the electron has to pass a *tight* ID filter. Additionally, both muons and electrons have to pass an offline p_T requirement to be greater than 27 GeV. Finally,

Process	Event Generator
$Z \to \tau\tau$	Powheg+Pythia8 and Sherpa
$Z \to ee$	Powheg+Pythia8
$Z \to \mu\mu$	Powheg+Pythia8
$W \to l\nu_l$	Powheg+Pythia8
$t\bar{t}$	Powheg+Pythia8
Single t	Powheg+Pythia8
Diboson	Powheg+Pythia8

Table 4: List of MC event generators used.

the opening angle between the two visible objects $\Delta\phi(\tau_h, l) \leq 2\pi/3$.

Events containing b-jets are vetoed in order to reject $t\bar{t}$ events. Also an isolation criterion is required to be passed by the leptons: for the muon (electron), the scalar sum of the p_T of the tracks within a cone of $\Delta R = 0.3(0.2)$ of the muon (electron) must be less than 0.06 times the muon (electron) p_T. Additionally, for the electron, the sum of the calorimeter cluster energy in a cone of size $\Delta R = 0.2$ must be 0.06 times smaller than the electron p_T. As we said in section 4.1, we expect signal events to peak around $\Omega = 1$, thus we select events where $\Omega \in (0, 1.4)$. Fig.12 shows the Ω distribution for $Z \to \tau_h \mu$ final state.
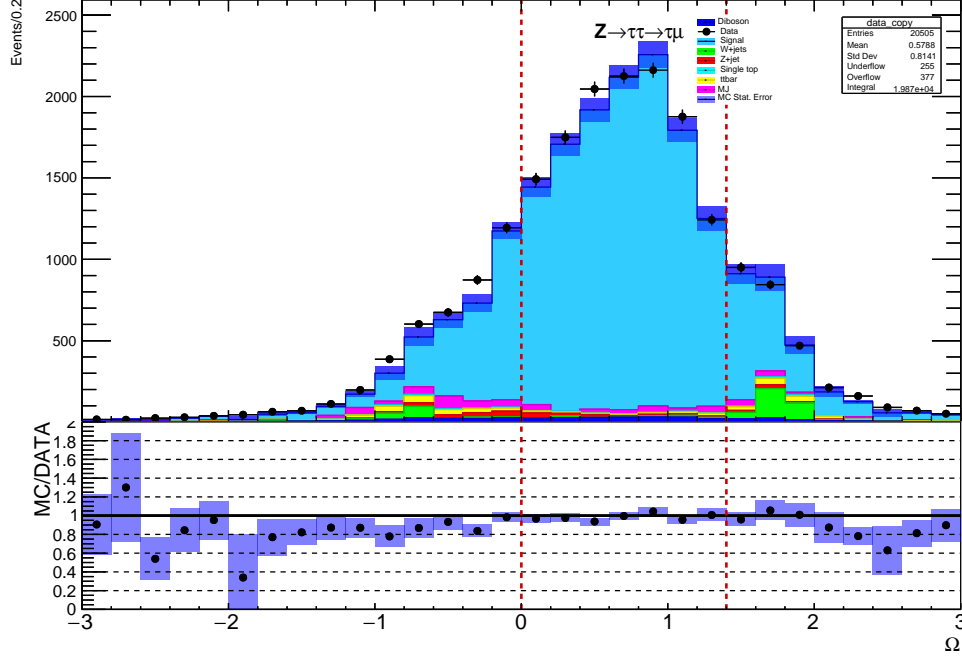
Figure 12: Distribution of Ω for $Z \to \tau_h \mu$ final state. All the other cuts have been applied apart from the one being plotted.The ATLAS data are shown as points with error bars, showing the statistical uncertainties. The detector-level predictions are shown as the shaded histograms, with the colour code as given on the plots.The region between the vertical dashed red lines is included in the final final candidate event sample by the selection criterion on the quantity plotted. The lower section of each plot shows the ratio of data to prediction. The uncertainties on the predictions represent the MC statistical uncertainties. These uncertainties are shown as blue shaded regions.

Additionally, a cut on the reconstructed invariant mass (m_{reco}) of the event is made, the cut aims to pick events where the invariant mass is around the Z boson mass ($70 \leq m_{\mathrm{reco}} \leq 110$ GeV). The invariant mass of the final states is calculated depending on the event topology. For events where $\Omega \in [0, 1]$ (*in-between events*),

$$m_{\mathrm{reco}}^2 = (q_l + q_{\tau_h} + q_{\nu_l} + q_{\nu_{\tau_h}})^2. \tag{34}$$

When the $\not{E}_T$ is outside (*outside events*),

$$(m_{\mathrm{reco}} - 5)^2 = (q_l + q_{\tau_h} + q_\nu)^2. \tag{35}$$

The RHS of Eq.(34) and Eq.(38) are vector sums, where q represents the four-momentum of each particle. In the outside events case we manually add 5 GeV to maintain our cuts consistent, since in this region we find empirically that the di-tau mass is underestimated and we wish to apply the same selection in both regions. Fig.13 shows the distribution of m_{reco} for the in-between and outside $Z \to \tau_h \mu$ events.
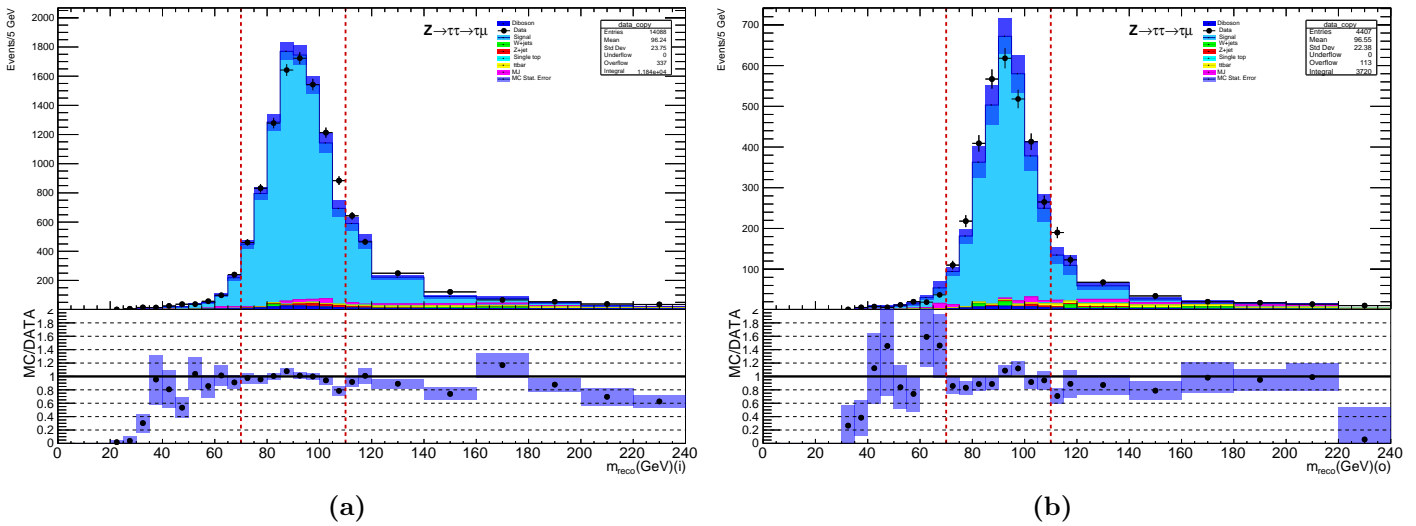
Figure 13: m_{reco} distribution for the in-between region (a) and the outside region (b). All the other cuts have been applied apart from the one being plotted.

In addition, for the $Z \to \tau_{\mathrm{h}} e$ final state, we add two cuts aimed to reject events where the τ_{h} candidate is faked by an electron. First to reject $Z \to ee$ events, a requirement on the invariant mass of the electron and τ_{h} candidate is made, $m(e, \tau_{\mathrm{h}}) < 80$ GeV. Then, we also make use of an ID algorithm trained to discriminate electrons from real τ_{h}. We require, eBDTScore≥ 0.06. The distributions for these variables are shown in Fig.14.
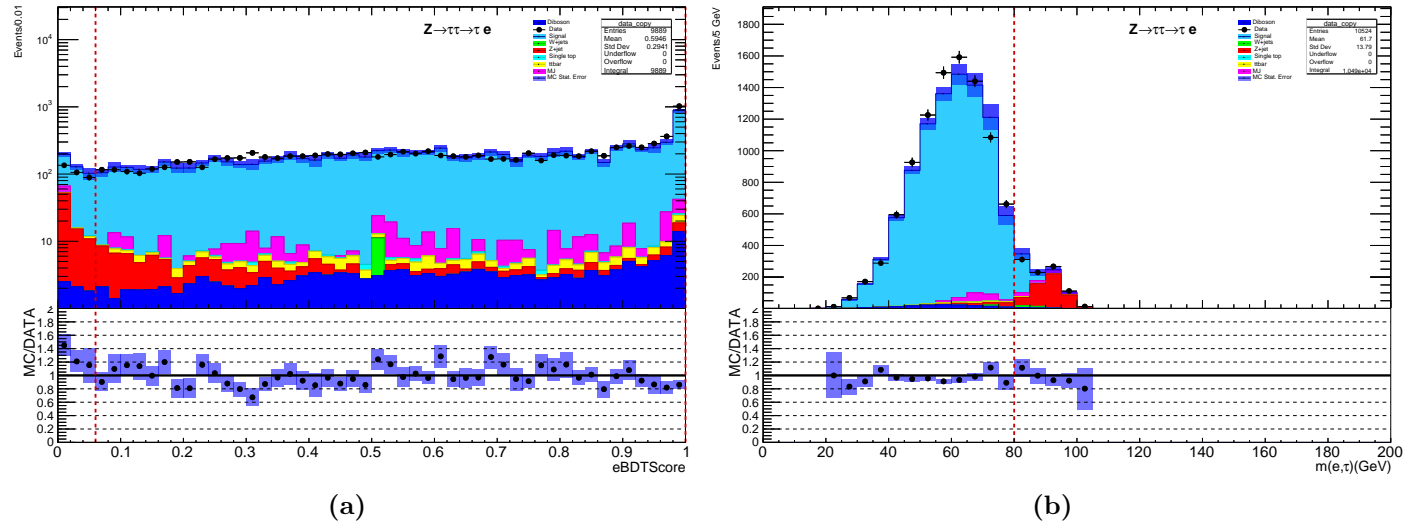
Figure 14: Distribution of the variables used for rejecting τ_{h} fakes coming from electrons. On the right $m(e, \tau_{\mathrm{h}})$ distribution (a) and on the left the eBDTScore distribution (b). All the other cuts have been applied apart from the one being plotted.

Finally, in order to measure the tau ID scale factors on the high-p_T region we select events where $p_T(\tau_{\mathrm{h}}) \geq 45$ GeV. The p_T distributions for τ_{h} candidates are shown in Fig.15 for the in-between and outside regions.
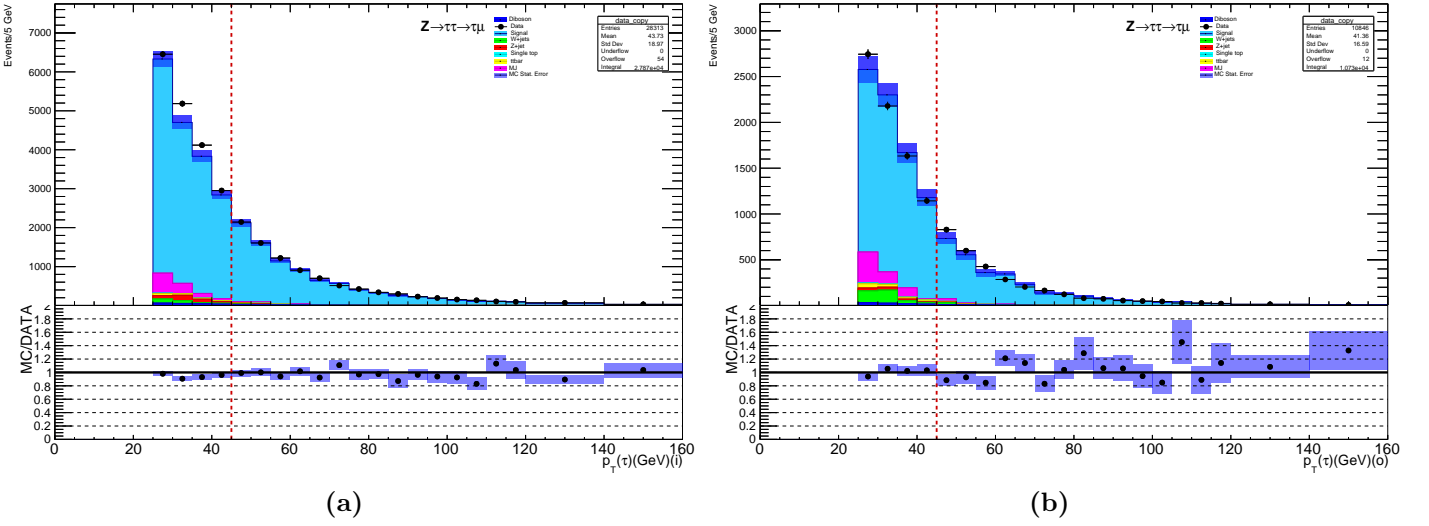
Figure 15: $p_T(\tau_h)$ distribution for the in-between (a) and outside (b) regions. All the other cuts have been applied apart from the one being plotted.

4.4 Multi Jet Background Estimation

As we said previously, τ_h candidates are seeded by jets, thus, QCD events represent a source of background. Nonetheless, we do not have MC simulations for this processes as compared with the EW interactions shown in Table 4. For this reason, we use a *data driven method* to estimate multi jet (MJ) background. For that purpose, we choose a variable that in principle we suppose is uncorrelated with the shape of the MJ background. For our study, this variable is the relative sign between the charges of the τ_h and the lepton. Thus, this defines two regions: the same sign (SS) region where $q(\tau_h) = q(l)$ and the opposite sign region where $q(\tau_h) = -q(l)$. Our estimate of MJ background for the SS region is obtained subtracting signal and electroweak backgrounds (EWBG) simulated contributions, basically:

$$\text{MJBG}_{\text{SS}} = \text{Data}_{\text{SS}} - \text{Signal}_{\text{SS}} - \text{EWBG}_{\text{SS}}, \tag{36}$$

To study the residual charge correlation, we define a control region (CR) where the MJ background is enhanced. This region is defined by events that fail either the lepton isolation criteria or the τ_h ID requirement of tauRNNScore$> 0.4\,(0.55)$ for 1-prong (3-prong) τ_h candidates and have the same other kinematic features of the signal region (SR) described in section 4.3. A diagram showing the four regions just defined is shown in Fig.16. Now, if charge correlation are the same in SR and CR, we have:

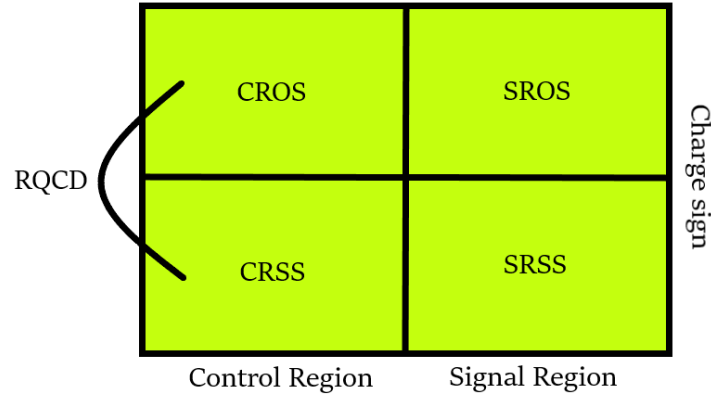$$\frac{\text{MJBG}_{\text{SROS}}}{\text{MJBG}_{\text{SRSS}}} = \frac{\text{MJBG}_{\text{CROS}}}{\text{MJBG}_{\text{CRSS}}}, \tag{37}$$

then,

$$\text{MJBG}_{\text{SROS}} = \text{MJBG}_{\text{SRSS}} \times \text{RQCD} \tag{38}$$

where $\text{RQCD} \equiv \frac{\text{MJBG}_{\text{CROS}}}{\text{MJBG}_{\text{CRSS}}}$. So, Eq.(38) gives the estimation of MJ background on the signal region (SROS).

Figure 16: Diagram showing the regions defined to estimate MJ background contribution in the SROS region. This data-driven method is also known as the ABCD method.

Table 5 summarises inputs into the calculation of the MJ background in the three candidate event samples.

Sample	$\mu\tau_h$	$e\tau_h$
CR OS Data	7396	6255
MC	6057	5031.9
CR SS Data	708	687
MC	191.3	279.2
RQCD	2.591	2.999
SR SS	212	219
MC	121.5	142.3
MJ Background	231.1 ± 41.8	230 ± 49.1

Table 5: Inputs into the calculation of the MJ background in the two final state candidate event samples $\mu\tau_h$ and $e\tau_h$. The numbers of data events in the CR OS and CR SS samples are given, together with the total numbers of events in these categories expected from MC. The excess of data with respect to MC is assumed to arise from MJ and is used to calculate the value of RQCD. The quoted uncertainties are statistical only.

5 Results

In this section we present the preliminary results of the performance of the τ_h identification algorithm using $\int \mathcal{L}dt = 139.2$ fb^{-1} of data recorded between 2015 and 2018. The correction factors are applied to simulation in order to match the efficiency observed in data. These correction factors are defined as the ratio between the efficiency measured in data and in simulation.

$$C_{\text{ID}} = \frac{\mathcal{E}_{\text{MC}}}{\mathcal{E}_{\text{Data}}}. \tag{39}$$

For this work, we present a preview of the value of the correction factors for *Tight* ID working point for τ_h candidates with p_T above 45 GeV. Since this report is about a work in progress and we have not studied yet the effect of the systematic uncertainties on our results, we will take another approach on estimating the correction factors.

5.1 Systematic uncertainties

The values for the systematic uncertainties used to report the value of the correction factors are presented in Table 6. These numbers have been provided by Terry Wyatt and Sam Dysch, based on their previous experience working on analysis that make use of $Z \to \tau_h l$ events.

Source	Sys. Uncertainty (%)
Electron ID efficiency	0.8
Muon ID Efficiency	0.2
Electron p_T scale and resolution	0.4
Muon p_T scale and resolution	0.3
Tau p_T scale	1.9
Electron trigger efficiency	0.1
Muon trigger efficiency	0.4
Integrated luminosity	1.7

Table 6: Systematic uncertainties used in this study.

5.2 $\mu\tau$ Final state

We define the simulation correction factor as

$$C_{\text{Tight-ID}} = \frac{N_{\text{MC}}}{N_{\text{Data}}}. \tag{40}$$

Where N_{DATA} are the total number of events measured in data substracting all the contributions from fake τ_h estimated in the MC and N_{MC} are the number of events in simulation that have a truth matched τ_h. The number of events that get selected after all the cuts and without the $p_T(\tau_h) > 45$ GeV requirement are shown in Table 7.

Samples	Before $p_\mathrm{T}(\tau_\mathrm{h})$>45 GeV cut	After all cuts
Z$\to\tau\tau$	34224.49±420.83(stat)±581.81(lumi)±675.88(sys)	11899.10±182.66(stat)±202.28(lumi)±234.99(sys)
Z+jets	543.21±11.06(stat)±9.23(lumi)±10.73(sys)	98.92±4.69(stat)±1.68(lumi)±1.95(sys)
W+jets	586.70±77.99(stat)±9.97(lumi)±11.59(sys)	37.11±18.75(stat)±0.63(lumi)±0.73(sys)
ttbar	339.94±6.84(stat)±5.78(lumi)±6.70(sys)	88.44±3.42(stat)±1.50(lumi)±1.75(sys)
Diboson	470.69±4.72(stat)±8.00(lumi)±9.30(sys)	187.07±2.82(stat)±3.18(lumi)±3.69(sys)
Single top	63.03±3.07(stat)±1.07(lumi)±1.24(sys)	14.35±1.50(stat)±0.24(lumi)±0.28(sys)
MJ	2386.06±143.76(stat)±40.56(lumi)±47.12(sys)	231.43±75.25(stat)±3.93(lumi)±4.57(sys)
MC Total	38634.12±668.27(stat)±656.78(lumi)±762.96(sys)	12556.42±289.09(stat)±213.46(lumi)±247.97(sys)
Data	39101±198(stat)±665(lumi)±772(sys)	12692±112(stat)±216(lumi)±251(sys)

Table 7: Number of selected events in data and each of the simulation samples in the $Z \to \tau_\mathrm{h}\mu$. Statistical and systematic uncertainties are presented separately. Luminosity uncertainty is presented apart. Z+jets stands for the combination of $Z \to ee$ and $Z \to \mu\mu$ samples.

The value obtained for $C_{\text{Tight-ID}}$ in the final state that contains one muon and a τ_h candidate is

$$C_{\text{Tight-ID}} = 0.989 \pm 0.012(\text{stat}) \pm 0.024(\text{lumi}) \pm 0.028(\text{sys}). \tag{41}$$

All the distributions of the relevant cuts for selecting our signal events after applying all the other cuts are shown in Fig.21 (Appendix A).

5.3 $e\tau$ Final state

For the final state that contains one electron and a τ_h candidate, the number of events that get selected after all the cuts and without the $p_\mathrm{T}(\tau_\mathrm{h}) > 45$ GeV requirement are shown in Table 8.

Samples	Before $p_\mathrm{T}(\tau_\mathrm{h})$>45 GeV cut	After all cuts
Z$\to\tau\tau$	25269.30±362.92(stat)±429.58(lumi)±531.26(sys)	8787.97±150.77(stat)±149.39(lumi)±184.76(sys)
Z+jets	682.15±12.69(stat)±11.60(lumi)±14.34(sys)	74.07±4.23(stat)±1.26(lumi)±1.56(sys)
W+jets	348.28±56.10(stat)±5.92(lumi)±7.32(sys)	8.08±8.08(stat)±0.14(lumi)±0.17(sys)
ttbar	255.55±6.05(stat)±4.34(lumi)±5.37(sys)	56.63±2.86(stat)±0.96(lumi)±1.19(sys)
Diboson	384.25±4.19(stat)±6.53(lumi)±8.08(sys)	152.92±2.58(stat)±2.60(lumi)±3.21(sys)
Single top	47.48±2.71(stat)±0.81(lumi)±1.00(sys)	11.29±1.32(stat)±0.19(lumi)±0.24(sys)
MJ	1530.54±101.21(stat)±26.02(lumi)±32.18(sys)	229.34±65.04(stat)±3.90(lumi)±4.82(sys)
Total	28487.55±545.87(stat)±484.29(lumi)±598.91(sys)	9320.31±234.87(stat)±158.44(lumi)±195.95(sys)
Data	29723±172(stat)±505(lumi)±625(sys)	9559±98(stat)±162(lumi)±201(sys)

Table 8: Number of selected events in data and each of the simulation samples in the $Z \to \tau_\mathrm{h}e$. Statistical and systematic uncertainties are presented separately. Luminosity uncertainty is presented apart.

The value obtained for $C_{\text{Tight-ID}}$ is

$$C_{\text{Tight-ID}} = 0.974 \pm 0.014(\text{stat}) \pm 0.023(\text{lumi}) \pm 0.029(\text{sys}). \tag{42}$$

All the distributions of the relevant cuts for selecting our signal events after applying all the other cuts are shown in Fig.22 (Appendix A).

5.4   Discussion

As this study makes use of events highly boosted in the transverse plane the $Z(p_T)$ modelling is very important. All the plots that have been shown in previous sections make use of the Sherpa generator for $Z \to \tau_h l$ events. Some distributions related to the $Z(p_T)$ are shown in Fig.17 for Sherpa. The complete set of plots showing the $Z(p_T)$ distribution for both e-tau and mu-tau final states for the two different type of topologies are shown in Fig.23 and Fig.24. In the first stages of our analysis we used Powheg+Pythia8 to simulate $Z \to \tau_h l$ events. Fig.18 shows the $Z(p_T)$ and $\Delta\phi(\tau_h, l)$ for the muon-tau final state for in-between events modelled by Powheg+Pythia8. As it can be seen the tendency in the MC is to underestimate the data for high-$Z(p_T)$ values. These results have been previously reported in ATLAS studies [39]. Fig.19 shows the $Z(p_T)$ modelling made by different generators. This has motivated us to use Sherpa to simulate our signal events.
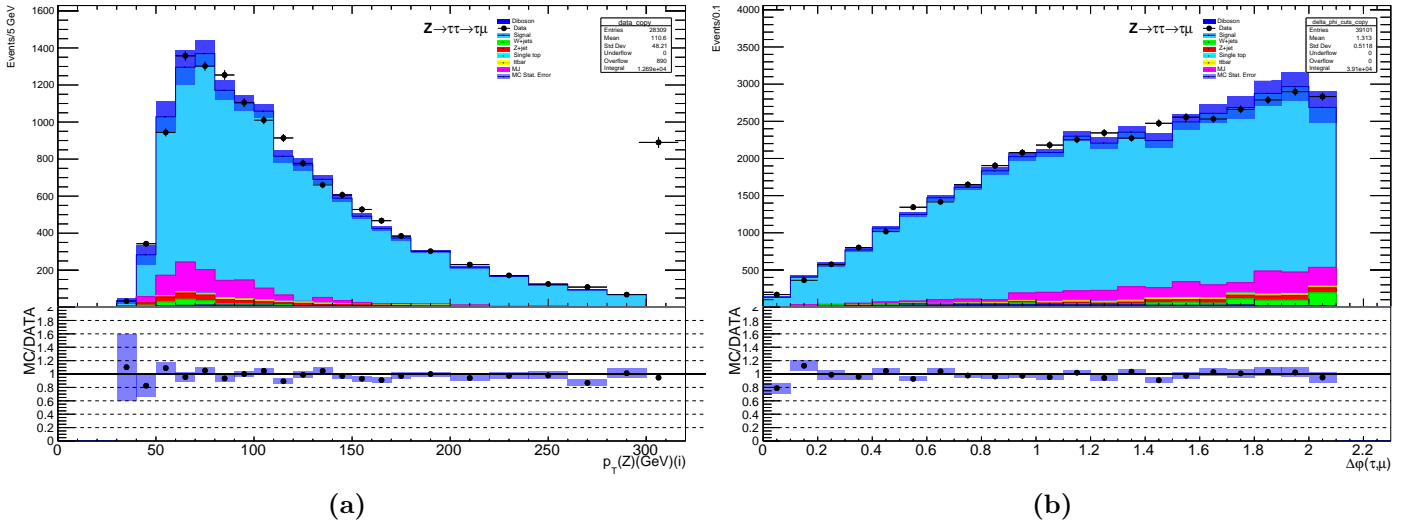
Figure 17: Distribution of $Z(p_T)$ for in-between events (a) and $\Delta\phi(\tau_h, l)$ (b) using Sherpa. All the other cuts have been applied apart from the one being plotted.
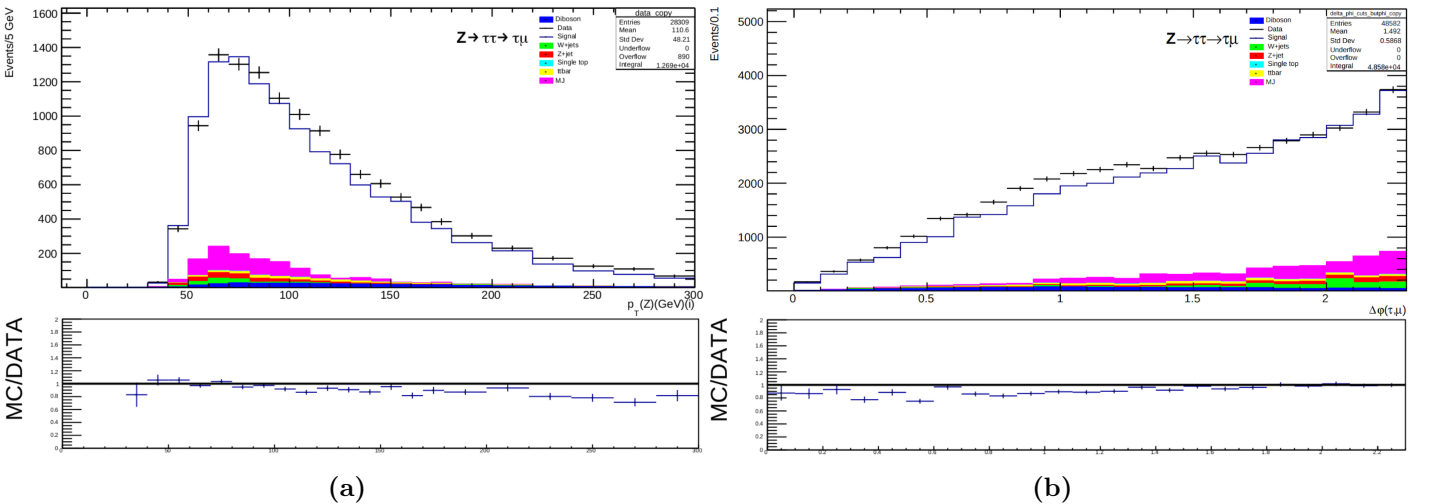

Figure 18: Distribution of $Z(p_T)$ for in-between events (a) and $\Delta\phi(\tau_h, l)$ (b) using Powheg+Pythia8. All the other cuts have been applied apart from the one being plotted.
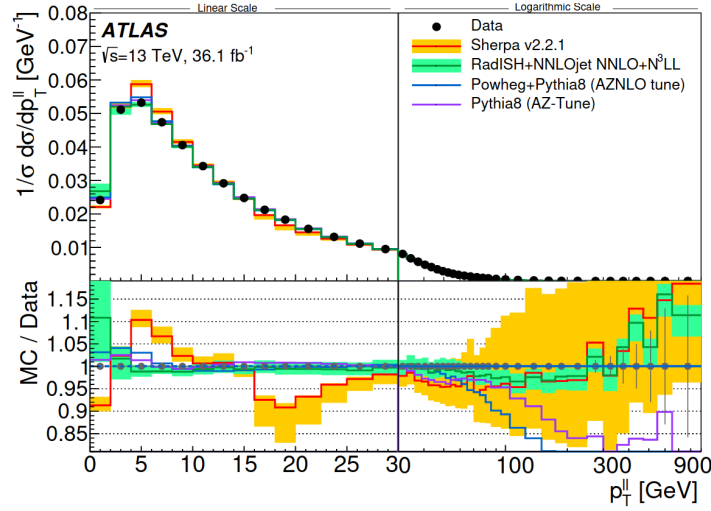
Figure 19: Comparison of the different modelling of the $Z(p_T)$ in Drell-Yan events made by different MC generators. As it can be seen Sherpa does a better job describing the Z boson transverse momentum for higher (p_T) values than Powheg+Pythia8. However both generators underestimate the measured value in the high-$Z(p_T)$ region. Taken from [39].

Another challenging task will be to control the MJ background contribution when we go to looser regions in tau-ID. As it can be seen in Fig.21c and Fig.21d the MJ background contribution starts to be more important for 1-prong and 3-prong taus for looser values of the RNN score. We have explored the possible correlation that could arise in actual $Z \to \tau_h l$ events in variables like the ratio between the transverse momentum of the tau and the lepton or the ratio between the $Z(p_T)$ and the leading jet. The distributions for this variables are shown in Fig.20a and Fig.20b respectively.

(a)

(b)
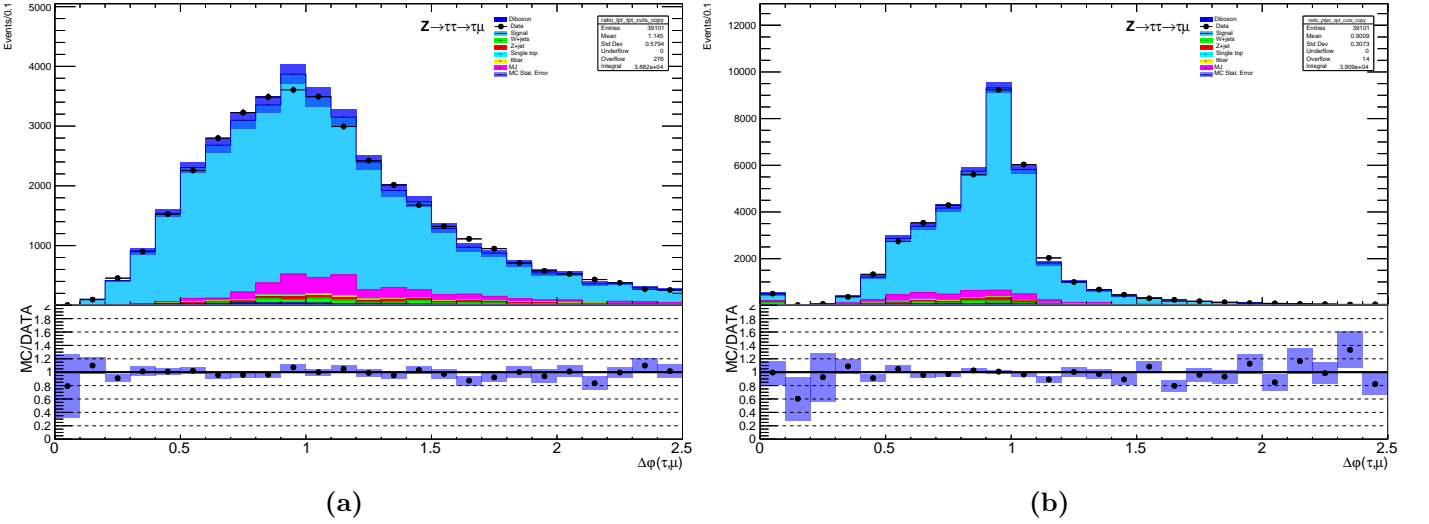
Figure 20: $r_{\frac{p_T(\mu)}{p_T(\tau)}}$ (a) and $r_{\frac{p_T(j)}{p_T(Z)}}$ distributions (b) do not seem to offer a big discriminating power against MJ background events.

These variables though do not offer a discriminating power against the MJ background.

6 Conclusions and prospects

The study presented is a work in progress. Given that the jets produced in hadronic tau decays have particular features, the ATLAS colaboration has developed algorithms to help with the identification of these decays. Simulation correction factors account for the difference in the efficiency of these algorithms between real data and simulation. The aim of our study is to derive the correction factors using $Z \to \tau_\mathrm{h} l = e, \mu$ events in a particular phase space where the τ_h are boosted in the transverse plane. A preliminary result of the value of the correction factor for the tight-ID working point is presented in this work.

The generators used for our study tend to underestimate the $Z(p_\mathrm{T})$ in the high momentum region. To correct for this effect we plan to reweight the MC predictions. This will offer us the possibility to derive the corrections factors for both generators and also claim a systematic uncertainty accounting for the $Z(p_\mathrm{T})$ modelling. Furthermore, in the future we will have to extend our study to the looser tau-ID working points. In this region the challenge will be to control the contribution coming from the MJ background.

Finally, we hope that all we have learnt about the highly boosted di-tau systems can be applied to a future analysis. The goal of this study will be to observe vector boson fusion production in final states with tau leptons. In this case the di-tau systems will recoil against the jets produced in the event. More information about previous observations of this topic can be find in [40, 41].

Bibliography

[1] M. Tanabashi, K. Hagiwara, Hikasa, et al. "Review of Particle Physics". In: *Phys. Rev. D* 98 (3 2018), p. 030001. DOI: 10.1103/PhysRevD.98.030001. URL: https://link.aps.org/doi/10.1103/PhysRevD.98.030001.

[2] Christopher Deutsch, Bertrand Martin dit Latour, and Christian Grefe. *Identification of hadronic tau lepton decays using neural networks in the ATLAS experiment.* Tech. rep. ATL-COM-PHYS-2019-773. RNN tau ID, ATL-PHYS-PUB-2019-033. Geneva: CERN, 2018. URL: https://cds.cern.ch/record/2680523.

[3] Murray Gell-Mann. "A Schematic Model of Baryons and Mesons". In: *Phys. Lett.* 8 (1964), pp. 214–215. DOI: 10.1016/S0031-9163(64)92001-3.

[4] S.L. Glashow and Steven Weinberg. "Breaking chiral symmetry". In: *Phys. Rev. Lett.* 20 (1968), pp. 224–227. DOI: 10.1103/PhysRevLett.20.224.

[5] Abdus Salam. "Weak and Electromagnetic Interactions". In: *Conf. Proc. C* 680519 (1968), pp. 367–377. DOI: 10.1142/9789812795915_0034.

[6] Steven Weinberg. "A Model of Leptons". In: *Phys. Rev. Lett.* 19 (1967), pp. 1264–1266. DOI: 10.1103/PhysRevLett.19.1264.

[7] Peter W. Higgs. "Broken Symmetries and the Masses of Gauge Bosons". In: *Phys. Rev. Lett.* 13 (16 1964), pp. 508–509. DOI: 10.1103/PhysRevLett.13.508. URL: https://link.aps.org/doi/10.1103/PhysRevLett.13.508.

[8] F. Englert and R. Brout. "Broken Symmetry and the Mass of Gauge Vector Mesons". In: *Phys. Rev. Lett.* 13 (9 1964), pp. 321–323. DOI: 10.1103/PhysRevLett.13.321. URL: https://link.aps.org/doi/10.1103/PhysRevLett.13.321.

[9] G. S. Guralnik, C. R. Hagen, and T. W. B. Kibble. "Global Conservation Laws and Massless Particles". In: *Phys. Rev. Lett.* 13 (20 1964), pp. 585–587. DOI: 10.1103/PhysRevLett.13.585. URL: https://link.aps.org/doi/10.1103/PhysRevLett.13.585.

[10] MissMJ Cush. *Standard model of elementary particles.* https://commons.wikimedia.org/wiki/File:Standard_Model_of_Elementary_Particles.svg, Last accessed on 2020-06-23. 2019.

[11] G. Arnison et al. "Experimental Observation of Isolated Large Transverse Energy Electrons with Associated Missing Energy at s**(1/2) = 540-GeV". In: *Phys. Lett. B* 122 (1983), pp. 103–116. DOI: 10.1016/0370-2693(83)91177-2.

[12] G. Arnison et al. "Experimental Observation of Lepton Pairs of Invariant Mass Around 95-GeV/c**2 at the CERN SPS Collider". In: *Phys. Lett. B* 126 (1983), pp. 398–410. DOI: 10.1016/0370-2693(83)90188-0.

[13] M. Banner et al. "Observation of Single Isolated Electrons of High Transverse Momentum in Events with Missing Transverse Energy at the CERN anti-p p Collider". In: *Phys. Lett. B* 122 (1983), pp. 476–485. DOI: 10.1016/0370-2693(83)91605-2.

[14] P. Bagnaia et al. "Evidence for $Z^0 \to e^+ e^-$ at the CERN $\bar{p}p$ Collider". In: *Phys. Lett. B* 129 (1983), pp. 130–140. DOI: 10.1016/0370-2693(83)90744-X.

[15] S. Schael et al. "Precision electroweak measurements on the Z resonance". In: *Phys. Rept.* 427 (2006), pp. 257–454. DOI: 10.1016/j.physrep.2005.12.006. arXiv: hep-ex/0509008.

[16] R.Keith Ellis, W.James Stirling, and B.R. Webber. *QCD and collider physics.* Vol. 8. Cambridge University Press, 2011. ISBN: 978-0-511-82328-2, 978-0-521-54589-1.

[17]   B. Abbott et al. "Differential production cross section of Z bosons as a function of transverse momentum at $\sqrt{s} = 1.8$ TeV". In: *Phys. Rev. Lett.* 84 (2000), pp. 2792–2797. DOI: 10.1103/PhysRevLett.84.2792. arXiv: hep-ex/9909020.

[18]   T. Affolder et al. "The transverse momentum and total cross section of e^+e^- pairs in the Z boson region from $p\bar{p}$ collisions at $\sqrt{s} = 1.8$ TeV". In: *Phys. Rev. Lett.* 84 (2000), pp. 845–850. DOI: 10.1103/PhysRevLett.84.845. arXiv: hep-ex/0001021.

[19]   M. L. Perl, Abrams, et al. "Evidence for Anomalous Lepton Production in $e^+ - e^-$ Annihilation". In: *Phys. Rev. Lett.* 35 (22 1975), pp. 1489–1492. DOI: 10.1103/PhysRevLett.35.1489. URL: https://link.aps.org/doi/10.1103/PhysRevLett.35.1489.

[20]   Michel Davier, Andreas Höcker, and Zhiqing Zhang. "The physics of hadronic tau decays". In: *Reviews of Modern Physics* 78.4 (2006), pp. 1043–1109. ISSN: 1539-0756. DOI: 10.1103/revmodphys.78.1043. URL: http://dx.doi.org/10.1103/RevModPhys.78.1043.

[21]   Antonio Pich. "Precision Tau Physics". In: *Prog. Part. Nucl. Phys.* 75 (2014), pp. 41–85. DOI: 10.1016/j.ppnp.2013.11.002. arXiv: 1310.7922 [hep-ph].

[22]   Enrico Fermi. "Tentativo di una Teoria Dei Raggi Beta". In: *Il Nuovo Cimento (1924-1942)* 11.1 (1932), pp. 669–688.

[23]   B.R. Martin and Graham Shaw. *Particle physics*. 1992.

[24]   S. Schael et al. "Electroweak Measurements in Electron-Positron Collisions at W-Boson-Pair Energies at LEP". In: *Phys. Rept.* 532 (2013), pp. 119–244. DOI: 10.1016/j.physrep.2013.07.004. arXiv: 1302.3415 [hep-ex].

[25]   Gregory Ciezarek et al. "A challenge to lepton universality in B-meson decays". In: *Nature* 546.7657 (2017), pp. 227–233. ISSN: 1476-4687. DOI: 10.1038/nature22346. URL: http://dx.doi.org/10.1038/nature22346.

[26]   Heavy Flavour Averaging Group. *Average of $R(D)$ and $R(D^\star)$ for Spring 2019*. 2019. URL: https://hflav-eos.web.cern.ch/hflav-eos/semi/spring19/html/RDsDsstar/RDRDs.html.

[27]   A. Airapetian et al. "ATLAS: Detector and physics performance technical design report. Volume 1". In: (1999).

[28]   Morad Aaboud et al. "Electron reconstruction and identification in the ATLAS experiment using the 2015 and 2016 LHC proton-proton collision data at $\sqrt{s} = 13$ TeV". In: *Eur. Phys. J. C* 79.8 (2019), p. 639. DOI: 10.1140/epjc/s10052-019-7140-6. arXiv: 1902.04655 [physics.ins-det].

[29]   Georges Aad et al. "Muon reconstruction performance of the ATLAS detector in proton–proton collision data at $\sqrt{s} = 13$ TeV". In: *Eur. Phys. J. C* 76.5 (2016), p. 292. DOI: 10.1140/epjc/s10052-016-4120-y. arXiv: 1603.05598 [hep-ex].

[30]   Matteo Cacciari, Gavin P. Salam, and Gregory Soyez. "The anti-k_t jet clustering algorithm". In: *JHEP* 04 (2008), p. 063. DOI: 10.1088/1126-6708/2008/04/063. arXiv: 0802.1189 [hep-ph].

[31]   "Optimisation and performance studies of the ATLAS b-tagging algorithms for the 2017-18 LHC run". In: (July 2017).

[32]   Morad Aaboud et al. "Reconstruction of primary vertices at the ATLAS experiment in Run 1 proton–proton collisions at the LHC". In: *Eur. Phys. J. C* 77.5 (2017), p. 332. DOI: 10.1140/epjc/s10052-017-4887-5. arXiv: 1611.10235 [physics.ins-det].

[33]   "Vertex Reconstruction Performance of the ATLAS Detector at $\sqrt{s} = 13$ TeV". In: (2015).

[34] Georges Aad et al. "ATLAS b-jet identification performance and efficiency measurement with $t\bar{t}$ events in pp collisions at $\sqrt{s} = 13$ TeV". In: *Eur. Phys. J. C* 79.11 (2019), p. 970. DOI: `10.1140/epjc/s10052-019-7450-8`. arXiv: `1907.05120 [hep-ex]`.

[35] Georges Aad et al. "Identification and energy calibration of hadronically decaying tau leptons with the ATLAS experiment in *pp* collisions at $\sqrt{s}$=8 TeV". In: *Eur. Phys. J. C* 75.7 (2015), p. 303. DOI: `10.1140/epjc/s10052-015-3500-z`. arXiv: `1412.7086 [hep-ex]`.

[36] Georges Aad et al. "Topological cell clustering in the ATLAS calorimeters and its performance in LHC Run 1". In: *Eur. Phys. J. C* 77 (2017), p. 490. DOI: `10.1140/epjc/s10052-017-5004-5`. arXiv: `1603.02934 [hep-ex]`.

[37] Sam Dysch. *QCD vs hadronic tau jets*. `https://github.com/sdysch/thesis_tikz_figures`, Last accessed on 2020-06-23. 2020.

[38] "Measurement of the tau lepton reconstruction and identification performance in the ATLAS experiment using *pp* collisions at $\sqrt{s} = 13$ TeV." In: (2017).

[39] Georges Aad et al. "Measurement of the transverse momentum distribution of Drell-Yan lepton pairs in proton-proton collisions at $\sqrt{s} = 13$ TeV with the ATLAS detector". In: (2019). arXiv: `1912.02844 [hep-ex]`.

[40] Georges Aad et al. "Measurement of the electroweak production of dijets in association with a Z-boson and distributions sensitive to vector boson fusion in proton-proton collisions at $\sqrt{s} = 8$ TeV using the ATLAS detector". In: *JHEP* 04 (2014), p. 031. DOI: `10.1007/JHEP04(2014)031`. arXiv: `1401.7610 [hep-ex]`.

[41] M. Aaboud et al. "Measurement of the cross-section for electroweak production of dijets in association with a Z boson in pp collisions at $\sqrt{s} = 13$ TeV with the ATLAS detector". In: *Phys. Lett. B* 775 (2017), pp. 206–228. DOI: `10.1016/j.physletb.2017.10.040`. arXiv: `1709.10264 [hep-ex]`.
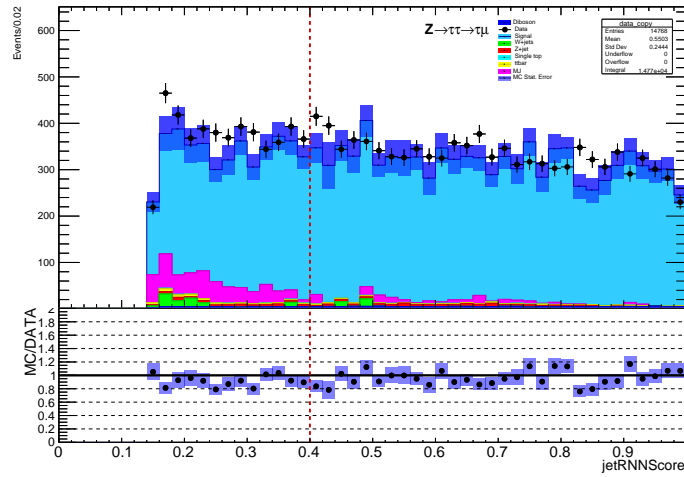
A Appendices

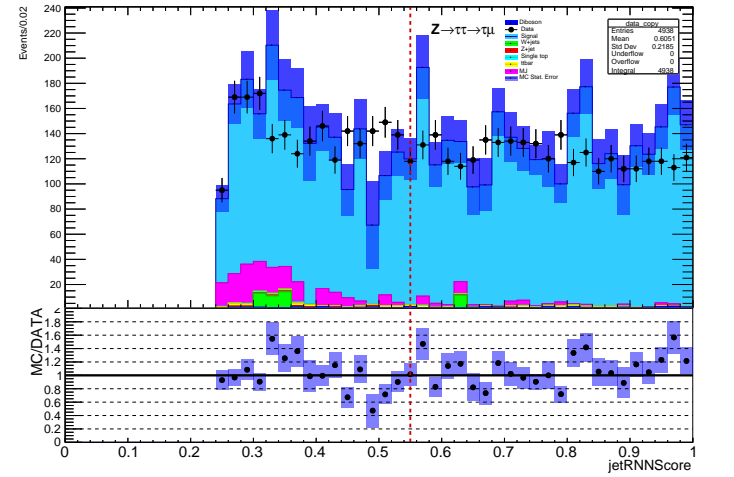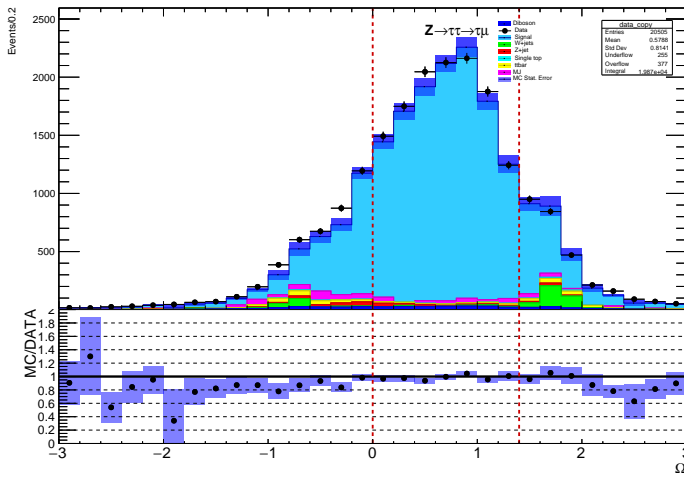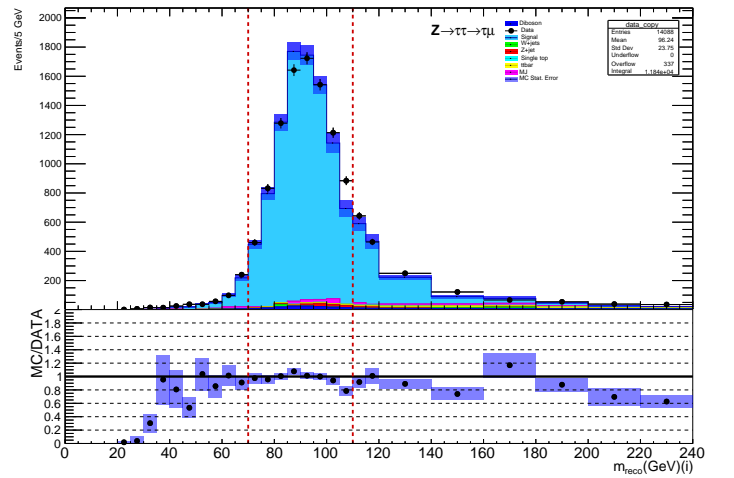## A.1 $Z \to \tau_{\text{h}}\mu$ final state distributions
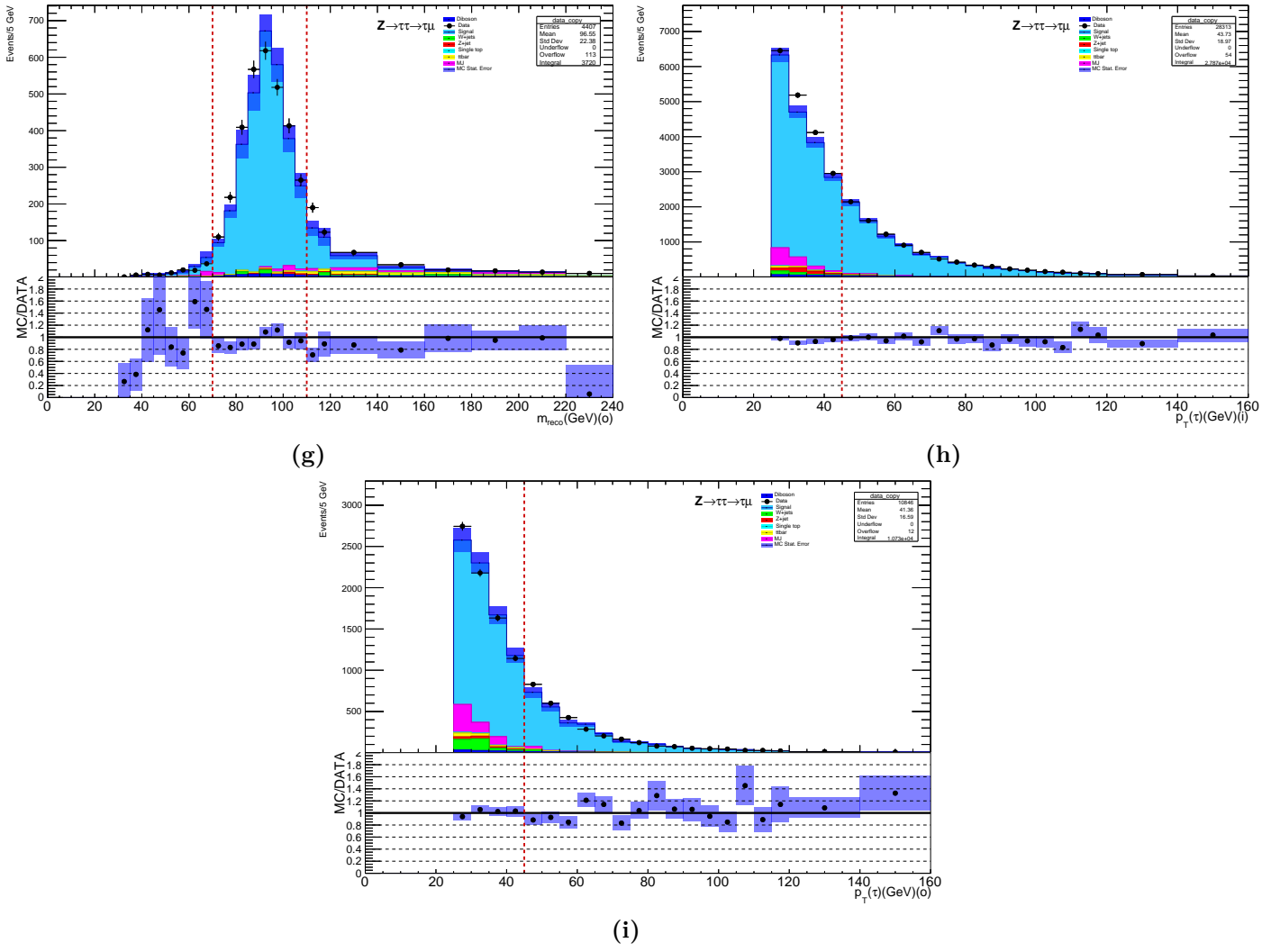

(a)

(b)

(c)

(d)

(e)

(f)

(g)

(h)

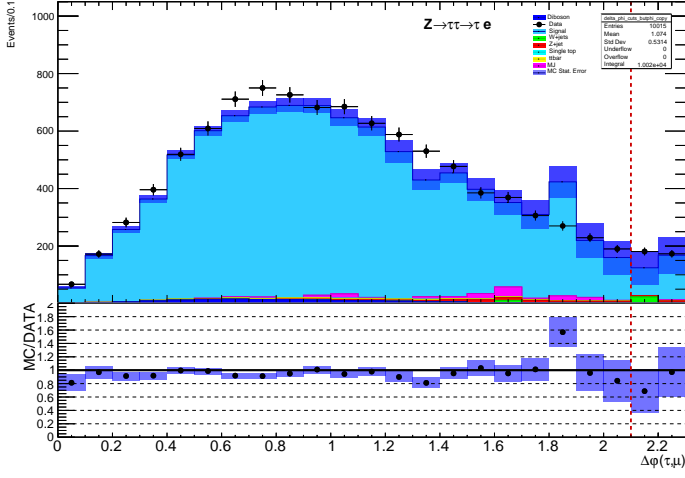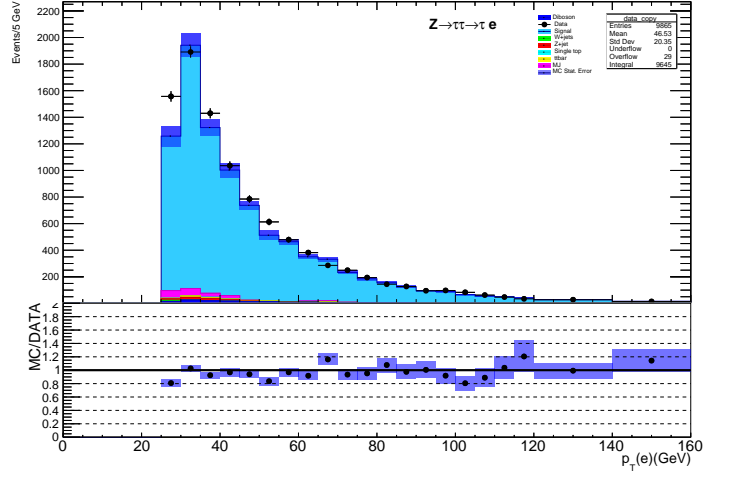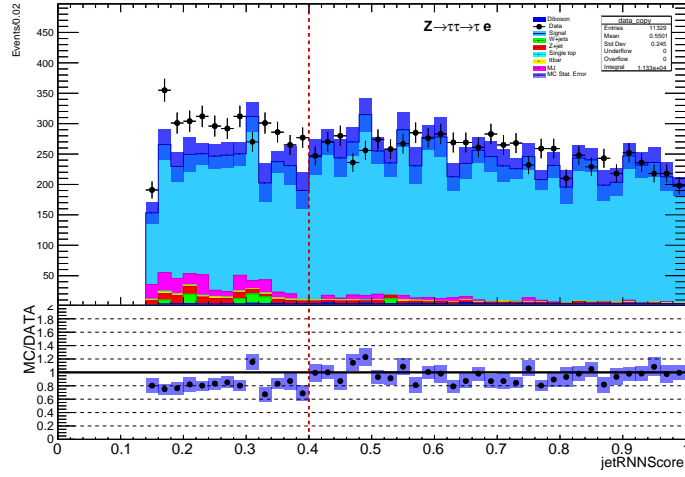**(i)**
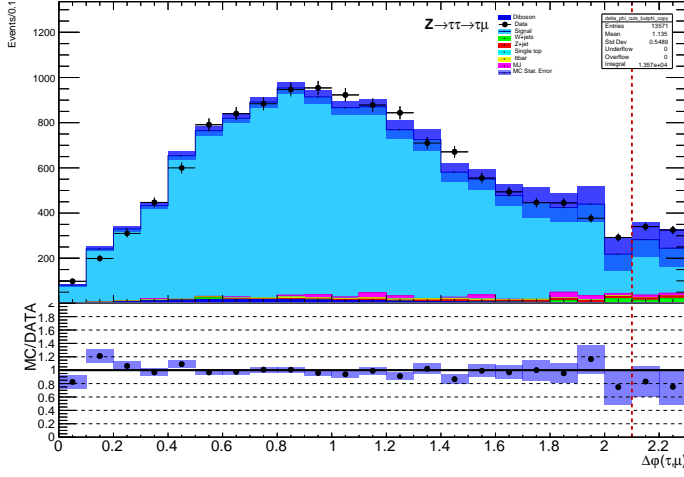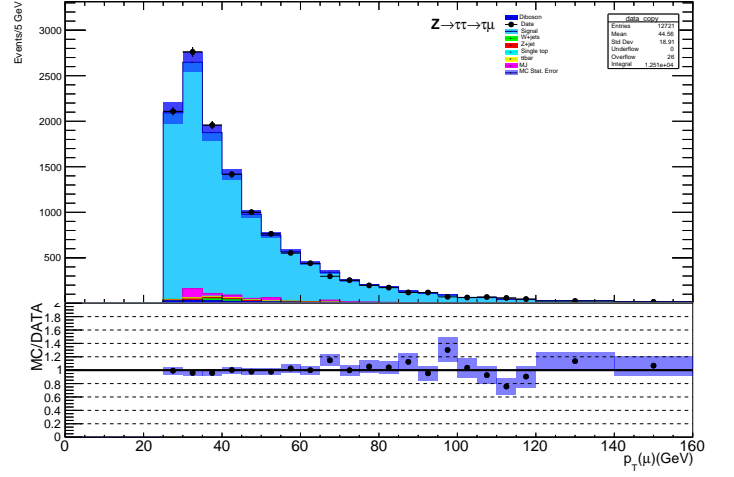
Figure 21: Distributions of all the variables used to select the signal events in the $Z \to \tau_\mathrm{h}\mu$ final state. In each plot all the cuts have been applied except for the one being displayed. The red vertical bars indicate the value of the cut. The distributions correspond to $\Delta\phi(\tau_\mathrm{h}, \mu)$ (a), $p_\mathrm{T}(\mu)$ (b), RNN score for 1-prong τ_h (c), RNN score for 3-prong τ_h (d), Ω (e), m_reco for in-between events (f), m_reco for outside events (g), $p_\mathrm{T}(\tau_\mathrm{h})$ for in-between events (h) and $p_\mathrm{T}(\tau_\mathrm{h})$ for outside events (i).

A.2 $Z \to \tau_h e$ final state distributions

(a)

(b)

(c)

(d)

(e)

(f)

(g)

(h)

(i)

(j)

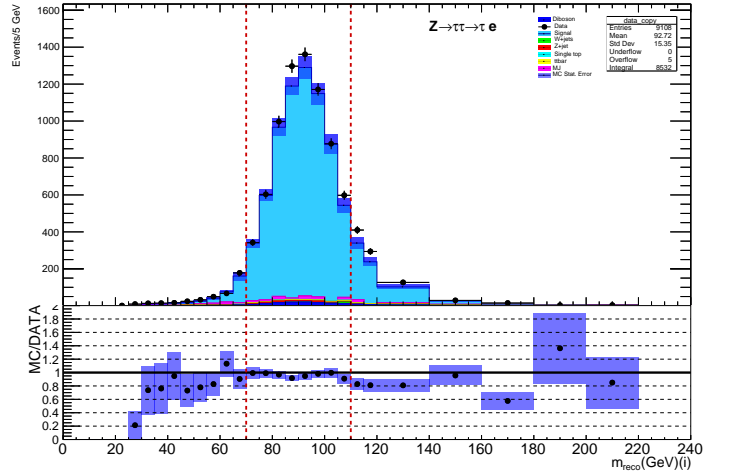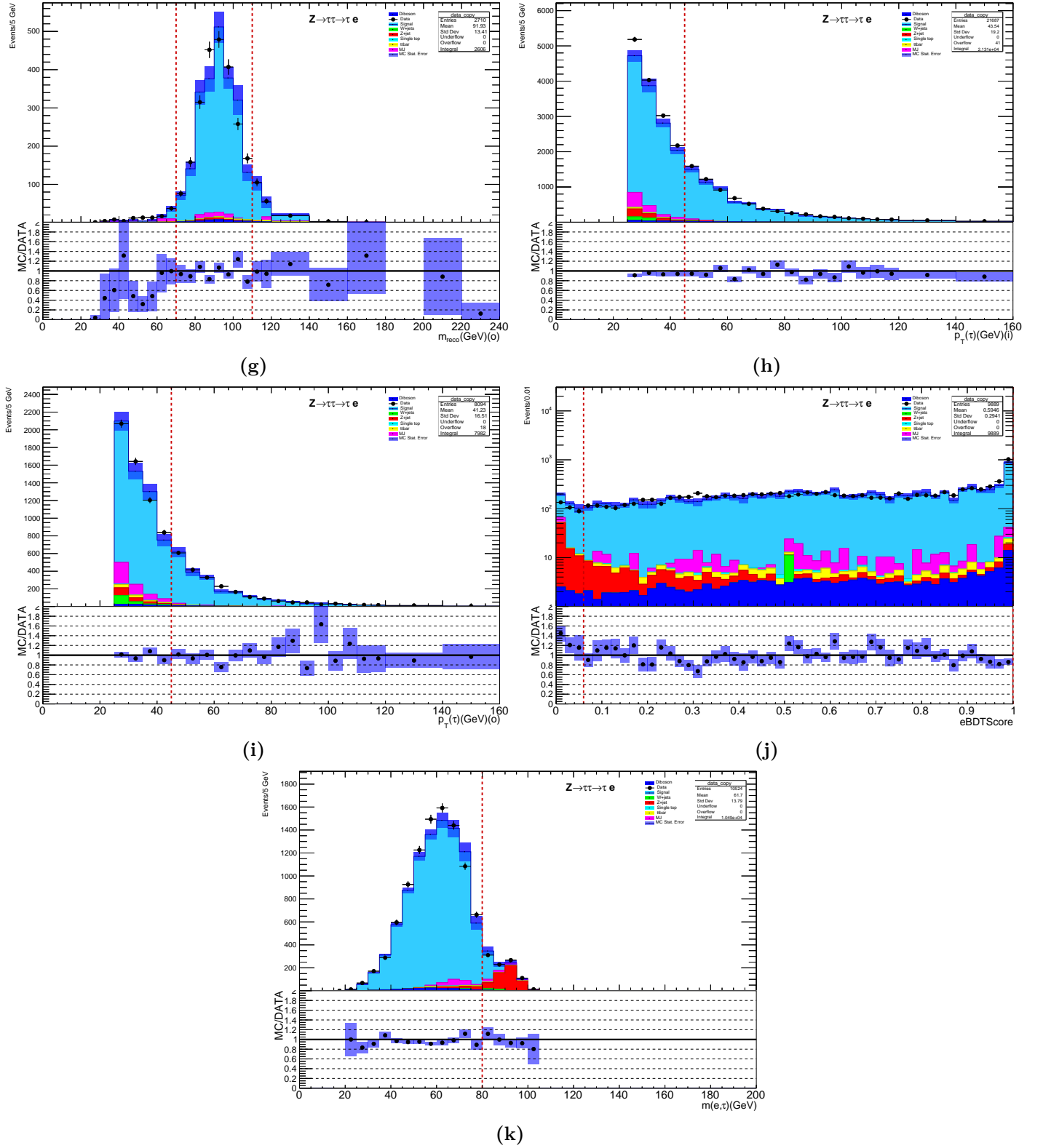**(k)**
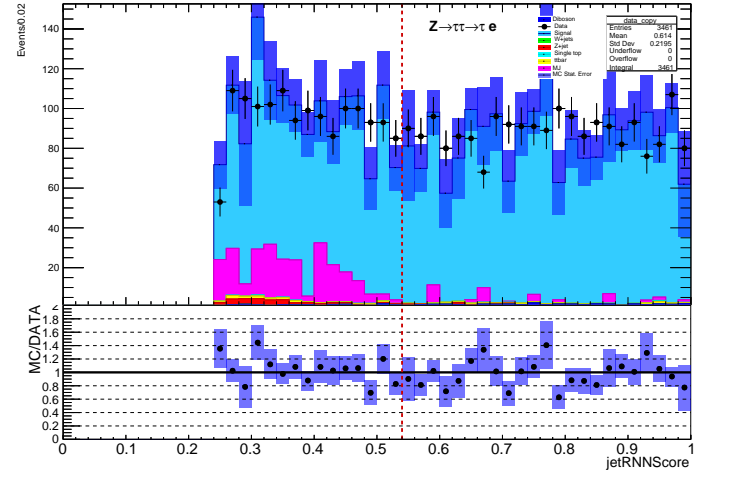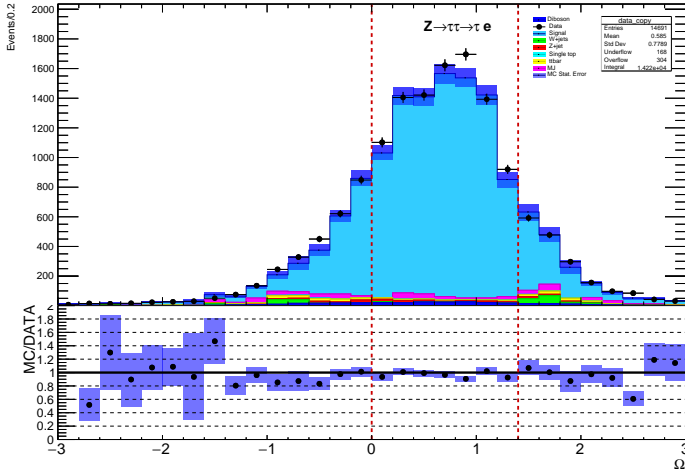
Figure 22: Distributions of all the variables used to select the signal events in the $Z \to \tau_\mathrm{h} e$ final state. In each plot all the cuts have been applied except for the one being displayed. The red vertical bars indicate the value of the cut. The distributions correspond to $\Delta\phi(\tau_\mathrm{h}, e)$ (a), $p_\mathrm{T}(e)$ (b), RNN score for 1-prong τ_h (c), RNN score for 3-prong τ_h (d), Ω (e), m_reco for in-between events (f), m_reco for outside events (g), $p_\mathrm{T}(\tau_\mathrm{h})$ for in-between events (h), $p_\mathrm{T}(\tau_\mathrm{h})$ for outside events (i), electron BDT score (j) and $m(\tau_\mathrm{h}, e)$ (k).

A.3 Zp_T distributions

(a)

(b)

(c)
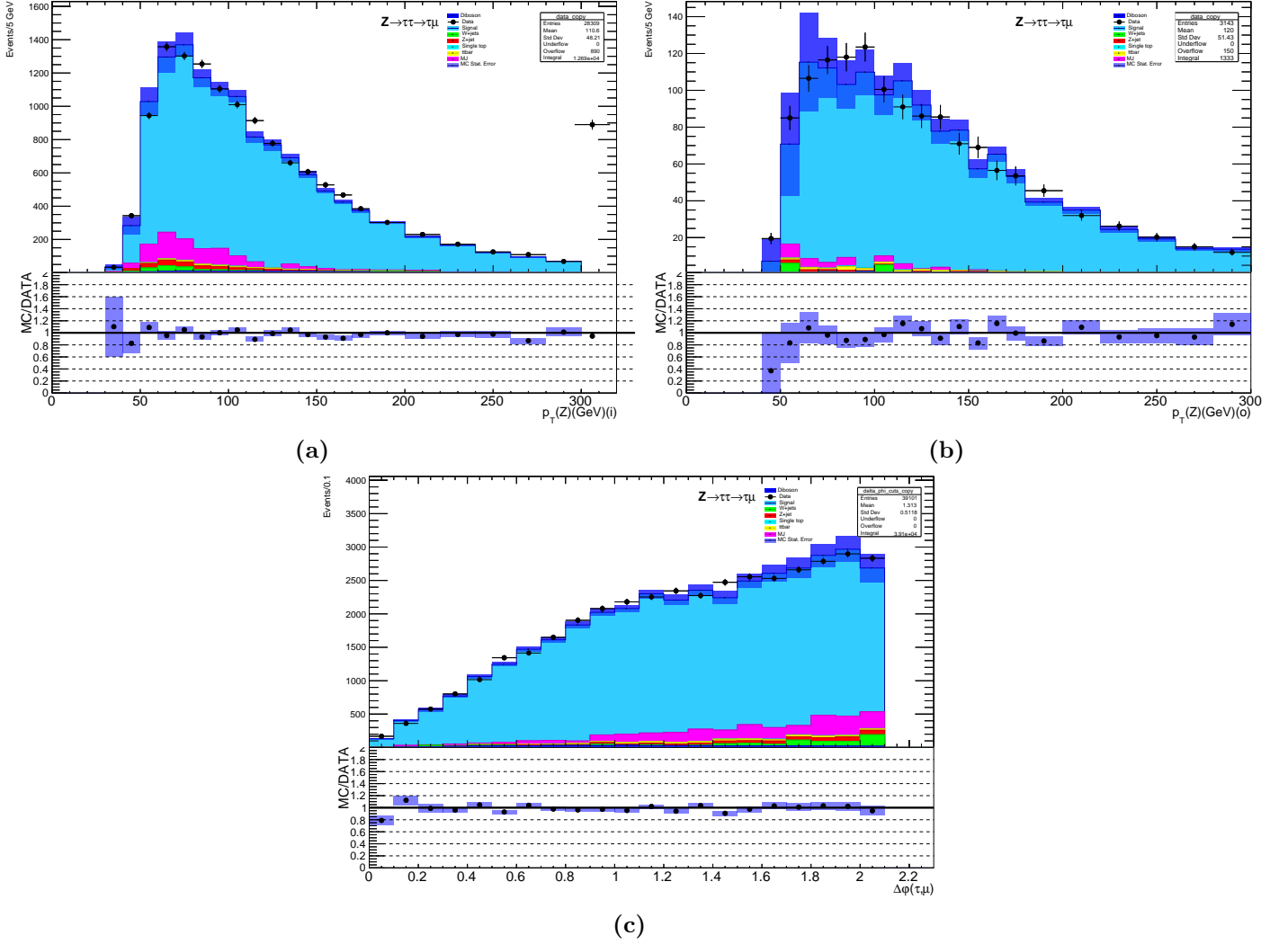
Figure 23: Distribution of Z(p_T) for in-between events (a), Z(p_T) for outside events (b) and $\Delta\phi(\tau_\mathrm{h}, \mu)$ (c). All the other cuts have been applied apart from the one being plotted.

(a)

(b)

(c)
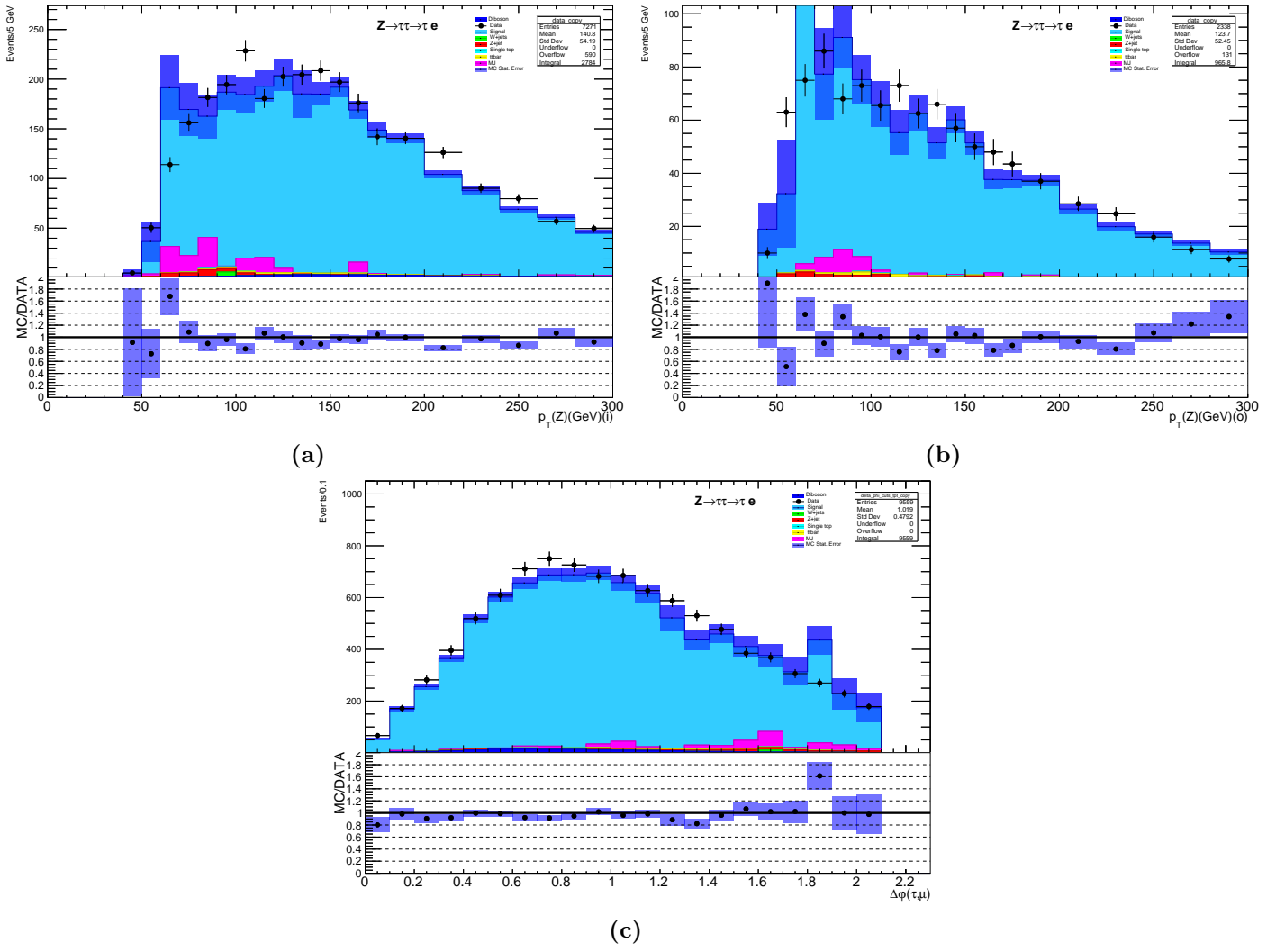
Figure 24: Distribution of $Z(p_T)$ for in-between events (a), $Z(p_T)$ for outside events (b) and $\Delta\phi(\tau_h, e)$ (c). All the other cuts have been applied apart from the one being plotted.